Jupiter's Unearthly Jets: A New Turbulent Model Exhibiting Statistical Steadiness without Large-Scale Dissipation*

STEPHEN I. THOMSON+ AND MICHAEL E. MCINTYRE

Department of Applied Mathematics and Theoretical Physics, University of Cambridge, Cambridge, United Kingdom

(Manuscript received 9 December 2014, in final form 24 September 2015)

ABSTRACT

A longstanding mystery about Jupiter has been the straightness and steadiness of its weather-layer jets, quite unlike terrestrial strong jets with their characteristic unsteadiness and long-wavelength meandering. The problem is addressed in two steps. The first is to take seriously the classic Dowling–Ingersoll (DI) $1\frac{1}{2}$-layer scenario and its supporting observational evidence, pointing toward deep, massive, zonally symmetric zonal jets in the underlying dry-convective layer. The second is to improve the realism of the model stochastic forcing used to represent the effects of Jupiter's moist convection, as far as possible within the $1\frac{1}{2}$-layer dynamics of the DI scenario. The real moist convection should be strongest in the belts where the interface to the deep flow is highest and coldest and should generate cyclones as well as anticyclones, with the anticyclones systematically stronger. The new model forcing reflects these insights. Also, it acts quasi frictionally on large scales to produce statistically steady turbulent weather-layer regimes without any need for explicit large-scale dissipation, and with weather-layer jets that are approximately straight thanks to the influence of the deep jets, allowing shear stability despite nonmonotonic potential vorticity gradients when the Rossby deformation length scale is not too large. Moderately strong forcing produces chaotic vortex dynamics and realistic belt–zone contrasts in the model's convective activity, through an eddy-induced sharpening and strengthening of the weather-layer jets relative to the deep jets, tilting the interface between them. Weak forcing, for which the only jet-sharpening mechanism is the passive, Kelvin shearing of vortices (as in the zonostrophic instability mechanism), produces unrealistic belt–zone contrasts.

1. Introduction

The aim of this work is to find the simplest stochastically forced model of Jupiter's visible weather layer that reproduces the straightness and steadiness of the observed prograde jets, and the belt–zone contrasts in small-scale convective activity, under a forcing regime that is arguably closer to the real planet's than either (i) the forcing used in orthodox beta-turbulence models or (ii) the purely anticyclonic forcing used in the recent work of Li et al. (2006) and Showman (2007). The new forcing is discussed below, after sketching the scientific background.

The weather layer is the cloudy moist-convective layer overlying a much deeper, hotter dry-convective layer. Such vertical structure, though not directly observed, is to be expected from the need to carry a substantial heat flux from below and from the basic thermodynamics and estimated chemical composition of Jupiter's atmosphere (e.g., Sugiyama et al. 2006, and references therein).

Even at high latitudes, the observed weather-layer jets are "straight" in the sense that, apart from small-scale disturbances, they closely follow parallels of latitude, especially the prograde jets, as clearly seen in the well-known animated polar view from *Cassini* images.[1] This extreme straightness contrasts with the meandering behavior found in many single-layer model studies, including the work of Li et al. (2006), Showman (2007), and, for instance, Scott and Polvani (2007). Jupiter's jets are also remarkably close to being steady, as evidenced by the almost identical zonal-mean zonal wind profiles seen

* Supplemental information related to this paper is available at the Journals Online website: http://dx.doi.org/10.1175/JAS-D-14-0370.s1.

+ Current affiliation: College of Engineering, Mathematics and Physical Sciences, University of Exeter, Exeter, United Kingdom.

Corresponding author address: Stephen I. Thomson, College of Engineering, Mathematics and Physical Sciences, University of Exeter, North Park Road, Exeter EX4 4QF, United Kingdom.
E-mail: stephen.i.thomson@gmail.com

[1] A movie is available from www.atm.damtp.cam.ac.uk/people/mem/nasa-cassini-index.html by kind courtesy of NASA and the *Cassini* mission (Porco et al. 2003, movie S1).

DOI: 10.1175/JAS-D-14-0370.1

in 1979 and 2000 from cloud tracking in the *Voyager 1* and *Cassini* images (Limaye 1986; Porco et al. 2003).

Because the weather layer appears turbulent and has no solid lower boundary, we confine attention to models that can reach statistically steady states without the large-scale friction used in the beta-turbulence models. We also avoid the use of large-scale Newtonian cooling as an eddy-damping mechanism. Real radiative heat transfer is not only far more complicated but also dependent on unknown details of the cloud structure within the weather layer and near the interface with the dry-convective layer.

The extreme straightness and steadiness of Jupiter's prograde jets make them strikingly dissimilar to the strong jets of Earth's atmosphere and oceans, with their conspicuous, large-amplitude long-wave meandering. By strong jets we mean the atmosphere's tropopause and polar-night jets and the strongest ocean currents, such as the Gulf Stream, the Kuroshio, and the Agulhas. The cores of these terrestrial strong jets are marked by concentrated isentropic gradients of Rossby–Ertel potential vorticity (PV) or gradients of ocean surface temperature, inversion of which implies sharp velocity profiles having width scales on the order of an appropriate Rossby deformation length scale L_D. Such meandering strong jets are quite different from the straighter but very weak topography-constrained "ghost" or "latent" jets in the Pacific Ocean, visible only after much time averaging (Maximenko et al. 2005, and references therein).

Jupiter's jets are hardly weak. On the contrary, at least some of them are strong enough to look shear unstable, by some criteria, with nonmonotonic potential-vorticity gradients (e.g., Dowling and Ingersoll 1989; Read et al. 2006; Marcus and Shetty 2011). Here we argue that their straightness and steadiness may come from a different, strictly extraterrestrial combination of circumstances, which calls for significant modeling innovations.

We propose a new idealized model whose two most crucial aspects are as follows. The first is the stochastic forcing of turbulence by thunderstorms and other small-scale moist-convective elements injected into the weather layer from the underlying dry-convective layer.[2] We assume that moist convection generates small cyclones and anticyclones, with a bias toward stronger anticyclones as measured by their potential-vorticity anomalies. Such a "PV bias" recognizes that heat as well as mass is injected. This contrasts with the mass-only, anticyclones-only forcing scenarios of Li et al. (2006) and Showman (2007) on the one hand and with the perfectly unbiased small-scale forcing used in beta-turbulence models on the other. PV bias will enable us to dispense with the large-scale friction required for statistical steadiness in beta-turbulence models.

The second aspect is the presence of zonally symmetric deep zonal jets in the underlying dry-convective layer. They will prove crucial to our model's behavior. Here we follow the pioneering work of Dowling and Ingersoll (1989, hereafter DI), who produced cloud wind evidence pointing to two remarkable and surprising conclusions. The first is that the large-scale vortex dynamics, in latitudes around 15°–35° at least, is approximately the same as the dynamics of a potential-vorticity-conserving 1½-layer model, with the upper layer representing the entire weather layer. DI's second conclusion is that the cloud wind data can be fitted into this picture only if the underlying dry-convective layer is in large-scale relative motion. The simplest possibility allowing a good fit is that the relative motion consists of deep zonally symmetric zonal jets. Those deep jets must have substantial velocities, comparable in order of magnitude to jet velocities at cloud-top levels. To our knowledge, no subsequent cloud wind study has overturned this second conclusion. So we use a 1½-layer model with deep jets. We treat the deep jets as prescribed and steady, consistent with the far greater depth and mass of the dry-convective layer.

The relevance of 1½-layer dynamics has recently gained support from a different direction. Sugiyama et al. (2014) present results from a two-dimensional cloud-resolving model that includes the condensation and precipitation of water and other minor species. A model weather layer emerges whose stable stratification is sharply concentrated near the interface with the dry-convective layer, as a consequence of water-cloud behavior. This result suggests that the real weather layer could be surprisingly close to the 1½-layer idealization with its perfectly sharp interface. Further such work is needed, if only because the real cloud-scale moist convection must be three-dimensional, as suggested by the morphology both of Jupiter's folded filamentary regions and of terrestrial supercell or "tornado alley" thunderstorms, with their intertwined patterns of updrafts, downdrafts, and precipitation.

DI's evidence for deep jets remains important today because, as yet, there are no other observational constraints on the existence or nonexistence of deep jets outside the equatorial region. No such constraints are

[2] We deliberately exclude other excitation mechanisms. In particular, we exclude terrestrial-type baroclinic instabilities. These are arguably weak or absent because of the absence of a solid lower surface at the base of the weather layer and because of the weak pole-to-equator temperature gradient—a weakness expected, in turn, from the well-known "convective thermostat" argument (Ingersoll and Porco 1978).

expected until, hopefully, gravitational data come in from the *Juno* mission in 2016. Numerical studies of the dry-convective layer cannot address the question because they need to make speculative assumptions about conditions at depth, including the effective bottom boundary conditions felt by Taylor–Proudman-constrained deep jets at latitudes within the associated tangent cylinder. Here there is great uncertainty. There is a range of possible conditions whose extremes are a slippery radiative layer well above the metallic-hydrogen transition, making deep jets easy to generate, and a no-slip magnetohydrodynamic transition layer that inhibits them (e.g., Guillot 2005; Jones and Kuzanyan 2009; Liu et al. 2013; Gastine et al. 2014, and references therein). Jupiter's prograde equatorial jet system needs separate consideration, being almost certainly outside any relevant tangent cylinder or cylinders.

Zonal symmetry or straightness is plausible for any deep, dry-convective jets that may exist, in virtue of the scale separation between the jets themselves and the relatively tiny, Coriolis-constrained convective elements that excite them, as seen in the numerical studies (e.g., Jones and Kuzanyan 2009; Gastine et al. 2014, and references therein).

Our own relatively modest aim, then, is to see whether, on the basis of the DI scenario with prescribed deep, straight jets, and nonmonotonic upper PV gradients, an idealized 1½-layer model with PV-biased forcing can produce not only statistical steadiness in the absence of large-scale dissipation but also realistic, quasi-zonal large-scale weather-layer structures, with moist-convective forcing strongest in the cyclonically sheared "belts" and weakest in the anticyclonically sheared "zones." The folded filamentary regions and lightning observed on the real planet, assumed to be symptomatic of moist convection, are concentrated in the belts (e.g., Porco et al. 2003). In addition we aim to test the effectiveness, within the idealized model, of the beta-drift-mediated migration of small anticyclones from belts into zones, following a suggestion by Ingersoll et al. (2000) that such migration might be significant.

We also look at the issue of shear instability and the relevance of Arnol'd's second stability criterion for nonmonotonic PV gradients (A2 stability), following suggestions by Dowling (1993) and Stamp and Dowling (1993). Jet straightness implies that the weather layer is either marginal or submarginal to shear instability; but the model results will force us to a stronger, and we believe novel, conclusion, differing from Dowling's original suggestion of marginal instability. Our conclusion is that the weather layer must be well *below* the threshold for marginal instability. In the model, at least, and probably on the real planet also, slight submarginality is insufficient to hold the jets realistically straight because it allows long-wave meandering to be too easily excited, even if not quite self-excited. Substantial submarginality with nonmonotonic PV gradients restricts L_D values to be substantially less than the jet spacing, as suggested schematically in the upper right of Fig. 1. A similar restriction probably holds on the real planet, constraining weather-layer depths and therefore abundances such as that of water. And the submarginality depends on having deep jets (section 6f below).

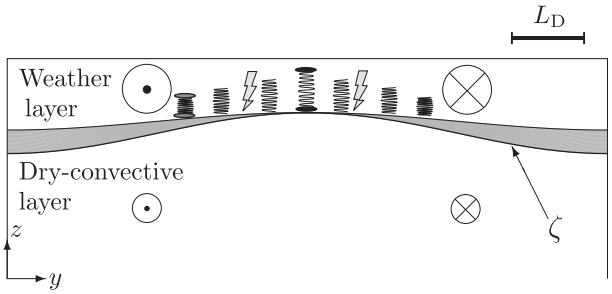

FIG. 1. Schematic of the model setup and motivation; see text. The bar at upper right indicates an L_D value well below the threshold for marginal shear instability with nonmonotonic upper PV gradients. The notional cumulonimbus clouds, concentrated in the model belt, can be thought of as tending to generate vortex pairs with cyclones below and anticyclones above. Such vortex pairs, called "hetons" or "heatons" in the oceanographic literature, can tilt and then propagate like ordinary two-dimensional vortex pairs. Ordinary vortex pairs are all that can be accommodated in a 1½-layer model. Ingersoll et al. (2000) remind us that "both cyclonic and anticyclonic structures exist within the belts" of the real planet and succinctly summarize the case for their being generated by moist convection.

The plan of the paper is as follows. Section 2 introduces the model. Section 3 introduces the PV-biased forcing and shows how it can act quasi frictionally. Section 4 motivates our choice of parameters, emphasizing those choices, including submarginal L_D, that lead to realistic, quasi-zonal weather-layer structures. Section 5 surveys the main body of results. Section 6 discusses the chaotic vortex-interaction mechanisms that produce realistic structures. We find that migration is crucial. By contrast, upscale energy cascades and the Rhines mechanism play no significant role, even though the flow is turbulent in the accepted chaotic dynamics sense. We also point out, in section 6d, that our model's quasi-frictional time scales are considerably shorter than the relevant radiative time scales, those near the interface in Fig. 1.

Section 7 shows that another mechanism—the Kelvin passive-shearing mechanism (Thomson 1887; Lord Kelvin), much discussed in recent years under the headings

second-order cumulant expansion (CE2), stochastic structural stability theory (SSST), and zonostrophic instability (ZI) (e.g., Srinivasan and Young 2014, and references therein)—has interesting effects but is unable to produce realistic weather-layer structures in our model. Section 8 presents some concluding remarks and suggestions for future work.

2. Model formulation

We use a doubly periodic, quasigeostrophic, pseudospectral β-plane version of the 1½-layer model, with leapfrog timestepping and a weak Robert filter. The model tries to mimic conditions in a band of Northern Hemispheric latitudes containing two deep jets, one prograde and one retrograde. The simplest way to achieve shear-stability properties resembling those of a horizontally larger domain (Thomson 2015, section 2.2.1) is to choose the model's zonal (x)-to-latitudinal (y) aspect ratio to be 2:1. In most runs a 512 × 256 spatial grid is used. Further detail is in Thomson (2015), and an annotated copy of the code is provided online through the authors' websites (http://emps.exeter.ac.uk/mathematics/staff/sit204/ and http://www.atm.damtp.cam.ac.uk/people/mem/).

Figure 1 shows schematically a meridional slice through the model, with the upper or weather-layer jets shown stronger than the deep jets and the interface correspondingly tilted, as dictated by thermal wind balance, with elevation ζ, say. The y axis points northward and the x axis points eastward, out of the paper. The central raised (i.e., cold) interface is in a model belt, cyclonically sheared, with model zones on either side and with the whole structure repeated periodically. The underlying dry-convective layer is modeled as adiabatic and infinitely deep, with constant potential temperature θ. The constant-θ interface with the weather layer is shown as the bottom of the shaded region. The interface is flexible and responsive to the dynamics. The shading is meant to indicate, in idealized form, the stable stratification suggested by the work of Sugiyama et al. (2014)—concentrated near the base of the weather layer, though less so in zones than in belts. Belt center is where the interface is highest, bringing it closest to the lifting condensation level for water. Such a configuration is consistent with thermal wind balance and with the standard perception that the weather layer's stable stratification—a positive vertical gradient $\partial\theta/\partial z$—results from moist convection with the convection strongest in the belts.

The model equations for $q(x, y, t)$, the weather layer's large-scale quasigeostrophic PV, with forcing $F(x, y, t)$ and small-scale dissipation $D(x, y, t)$, are

$$\left(\frac{\partial}{\partial t} + \mathbf{u}\cdot\nabla\right) q = F + D; \tag{2.1}$$

$$q := \nabla^2\psi + \beta y - k_D^2(\psi - \overline{\psi}_{\text{deep}}). \tag{2.2}$$

Here ∇^2 is the two-dimensional Laplacian in the x–y plane, β is the local latitudinal gradient of the vertical component of the planetary vorticity, k_D is the reciprocal of the Rossby deformation length L_D based on the weather layer's mean depth and on the reduced gravity at the interface; $\psi(x, y, t)$ and $\mathbf{u}(x, y, t)$ are the geostrophic streamfunction and velocity for the weather layer, such that $\mathbf{u}$ is horizontal with components $\mathbf{u} = (u, v) = (-\partial\psi/\partial y, \partial\psi/\partial x)$, and $\overline{\psi}_{\text{deep}}$ is the geostrophic streamfunction for the prescribed steady, zonally symmetric zonal flow ($\overline{u}_{\text{deep}} = -\partial\overline{\psi}_{\text{deep}}/\partial y$) in the dry-convective layer. In (2.1), D is a quasi-hyperdiffusive dissipation in the form of a high-wavenumber spectral filter, used only to maintain grid-scale numerical stability. It will be ignored in most of the theoretical discussion. We adopt the filter described in appendix B of Smith et al. (2002). The model code evaluates $\nabla\psi$ and ∇q in spectral space before fast Fourier transforming to physical space and evaluating $\mathbf{u}\cdot\nabla q$ by pointwise multiplication, then transforming back.

Following Dowling (1993) and Stamp and Dowling (1993), we somewhat arbitrarily take the deep flow to have a sinusoidal profile

$$\overline{u}_{\text{deep}}(y) = U_0 + U_{\max}\sin\left(\frac{y}{L}\right), \tag{2.3}$$

where U_0 and $U_{\max}$ are constants. The length scale L is $(2\pi)^{-1}$ times the domain's y period, the full wavelength of the jet spacing, which we fix at 10 000 km to represent midlatitude conditions.

The real deep-jet profiles may of course be different. However, they are not well known. DI's analysis did, to be sure, find rounded $\overline{u}_{\text{deep}}(y)$ profiles, in striking contrast with the sharper profiles found in some dry-convective models. However, DI's cloud wind analysis may not have been accurate enough to fix $\overline{u}_{\text{deep}}(y)$ with great precision. While cloud wind analyses have greatly improved since then—see especially Asay-Davis et al. (2009)—we are not aware of any corresponding published estimates of $\overline{u}_{\text{deep}}(y)$ profiles and their error bars.

With the exception of q, which contains the non-periodic terms $\beta y - k_D^2 U_0 y$, all the model's weather-layer fields are assumed to be doubly periodic, including the streamfunction ψ and the zonal-mean gradient of q,

$$\frac{\partial\overline{q}}{\partial y} = \beta - \frac{\partial^2\overline{u}}{\partial y^2} + k_D^2(\overline{u} - \overline{u}_{\text{deep}}). \tag{2.4}$$

The periodicity of ψ entails that

$$\int_0^{2\pi L} \overline{u}\, dy = 0, \tag{2.5}$$

which implicitly assumes not only that we are in a particular reference frame but also that the domain-averaged angular momentum budget is steady.[3] And without loss of generality we may take the domain integrals of ψ and F to vanish:

$$\iint \psi\, dx\, dy = 0 \quad \text{and} \quad \iint F\, dx\, dy = 0. \tag{2.6}$$

The first of these follows from the freedom to add an arbitrary function of time t alone to the streamfunction ψ with no effect on the quasigeostrophic dynamics. Physically, this says that a small variation in the total mass of the weather layer, due, for instance, to horizontally uniform diabatic processes, has no dynamical effect as long as the mean weather-layer depth, hence L_D value, can be considered constant to leading order in Rossby number. From (2.2) and the first equation of (2.6), we then have

$$\frac{\partial}{\partial t} \iint q\, dx\, dy = 0, \tag{2.7}$$

which is consistent with (2.1) only if the second equation of (2.6) also holds. This can be seen by domain integrating the flux form of (2.1) and noting that $\overline{v} = \partial\overline{\psi}/\partial x = 0$ and that $\iint D\, dx\, dy = 0$ in virtue of D's restriction to the highest wavenumbers. It is convenient to view (2.7) as a quasigeostrophic counterpart to the ''impermeability theorem'' for the exact, Rossby–Ertel PV (e.g., Haynes and McIntyre 1990).

From here on, we ignore the small-scale dissipation D. The zonal-mean dynamics is then described by

$$\frac{\partial \overline{q}}{\partial t} = -\frac{\partial(\overline{v'q'})}{\partial y} + \overline{F}, \tag{2.8}$$

where the primes denote departures from zonal averages $\overline{(\ )}$. The model's Taylor identity (e.g., Bühler 2014), which allows the mean PV dynamics to be translated into mean momentum dynamics, if desired,[4] is

$$\frac{\partial(\overline{u'v'})}{\partial y} = -\overline{v'q'}. \tag{2.9}$$

The Taylor identity is a consequence of (2.2) alone, as is easily verified using $\partial\overline{(\ )}/\partial x = 0$, hence valid at all eddy amplitudes and independent of forcing and dissipation. By multiplying (2.1) by $-\psi$ and continuing to ignore D, we find the relevant energy equation to be

$$\frac{\partial E}{\partial t} = -\iint \psi F\, dx\, dy, \tag{2.10}$$

where E is the kinetic plus available potential energy of the weather layer—the model's only variable energy—divided by the mass per unit area. That is,

$$E := \iint \left(\frac{1}{2}|\nabla\psi|^2 + \frac{1}{2}k_D^2\psi^2\right) dx\, dy. \tag{2.11}$$

3. The stochastic forcing F

a. *Impulsive injection of small vortices*

The forcing F corresponds to repeated injections of close-spaced, east-to-west-oriented pairs of small vortices at random locations and in alternating order, cyclone–anticyclone alternating with anticyclone–cyclone. In each pair, the cyclone is weaker than the anticyclone by a fractional amount b, say, which we call the ''fractional bias'' and which increases with vortex strength so as to express the notion that the dry-convective layer supplies the weather layer with mass and heat, but with relatively more mass in the stronger convection events. Each vortex is impulsively injected using a parabolic PV profile; see (3.1) and inset to Fig. 2 below.

We acknowledge that this must be an exceedingly crude representation of vortex generation by the real three-dimensional convection, whose structure and tangled vortex-line topology are unknown and have yet to be plausibly modeled. A simplistic vortex-injection scheme may be the best that can be done within the 1½-layer dynamics and indeed is a rather time-honored idea (e.g., Vallis et al. 1997, section 3b; Li et al. 2006; Showman 2007; Humphreys and Marcus 2007, section 5a and Fig. 6). Within such a scheme, it is arguably most realistic to use vortices of both signs, avoiding the anticyclones-only scenarios that might be suggested by too exclusive a focus on cloud-top observations and which, in any case, would correspond to mass injection only.

We use east-to-west-oriented pairs for two reasons. One is to make zonally averaged quantities such as $\overline{q}$

[3] In other words, any domain-averaged external zonal force is either negligible or balanced by a domain-averaged ageostrophic mean y velocity.

[4] The mean momentum dynamics is given by the minus the indefinite y integral of (2.8), in which $\int dy(k_D^2\partial\overline{\psi}/\partial t + \overline{F})$ represents minus the Coriolis force from the ageostrophic mean y velocity, whose y derivative is related via mass conservation to layer-depth changes and to the forcing $\overline{F}$ conceived of as mass injection or withdrawal.

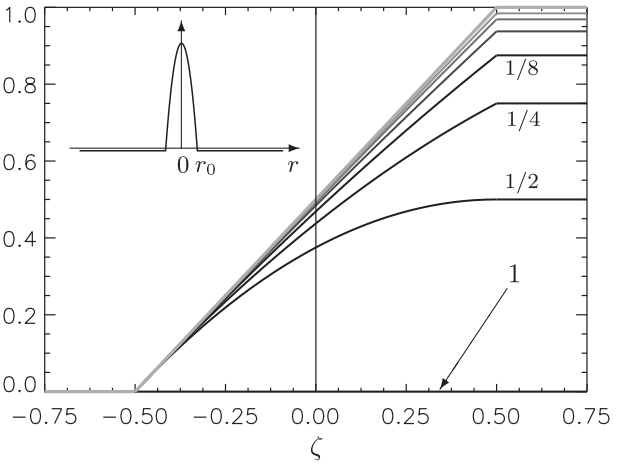

FIG. 2. Functions used in the vortex-injection scheme. The inset at upper left shows the $\Delta q(r)$ profile for an injected cyclone of radius $r_0 \ll L_D$, discussed in (3.1)ff. The top, light-colored curve in the main figure shows the function $\rho(\zeta)$ defined in (3.8), equivalently $|q_{\mathrm{pkA}}|/q_{\max}$ when the choice (3.9) is made. The remaining curves show $q_{\mathrm{pkC}}/q_{\max}$ for different nonzero biases, according to (3.6)–(3.9) and the text below (3.6). From bottom up, we have $b = 1$ ($q_{\mathrm{pkC}} = 0$ for all ζ) and then $q_{\mathrm{pkC}}/q_{\max}$ for $b_{\max} = 1/2, 1/4, 1/8, 1/16, 1/32$, and $1/64$. Note, however, that (3.9) is used subject to the further conditions described in (3.10)ff.

and $\overline{v'q'}$ less noisy. The other, less obvious, reason is an interest in assessing whether the Kelvin/CE2/SSST/ZI passive-sheared-disturbance mechanism has a significant role in any of the regimes we find. The Kelvin mechanism operates when the injected vortices are so weak that they are passively sheared by the mean flow $\overline{u}(y)$, producing systematically slanted structures and hence Reynolds stresses $\overline{u'v'}$ that can cause jet self-sharpening.

The Kelvin mechanism is entirely different from the inhomogeneous-PV-mixing mechanism that produces terrestrial strong jets through drastic piecewise rearrangement of a background PV gradient. It is also different from the Rhines mechanism, in which the injected vortices are strong enough to undergo the usual vortex interactions, especially the vortex merging that produces an upscale energy cascade that is then arrested, or slowed, by the Rossby wave elasticity of an *unrearranged*, uniform background PV gradient. We are, of course, interested in whether any of these mechanisms have significant roles. Regarding the Kelvin mechanism, it is strongest when the forcing is anisotropic in the sense of east-to-west vortex-pair orientation (e.g., Shepherd 1985; Srinivasan and Young 2014). So our choice of east-to-west orientation will give the Kelvin mechanism its best chance.

The impulsive vortex injections, corresponding theoretically to temporal delta functions in the forcing function F, are actually spread over time intervals $2\Delta t$ to avoid exciting the leapfrog computational mode, where Δt is the time step. This is still fast enough for advection to be negligible, implying that the injections are instantaneous to good approximation. The parabolic profile of the resulting change $\Delta q(r)$ in the PV field is given by

$$\Delta q(r) = q_{\mathrm{pk}}\left(1 - \frac{r^2}{r_0^2}\right), \quad r \le r_0, \tag{3.1}$$

the peak vortex strength q_{pk} being positive for a cyclone and negative for its accompanying anticyclone. The relative radius $r := |\mathbf{x} - \mathbf{x}_c|$, with $\mathbf{x} = (x, y)$ denoting horizontal position and $\mathbf{x}_c = (x_c, y_c)$ the position of the vortex center. The radius r_0 is taken as small as we dare, consistent with reasonable resolution and realistic-looking vortex interactions (Thomson 2015, sections 2.1.1 and 3.5.2). In most cases $r_0 = 4\Delta x$, where Δx is the grid size.

b. *The complementary forcing*

Thanks to the peculiarities of quasigeostrophic dynamics and to our model choices we need the forcing to satisfy the second equation in (2.6). The model code does this automatically by assigning zero values to all spectral components having total wavenumber 0. The most convenient way to see what it means, however, is to think of each injected vortex as satisfying the second equation in (2.6) individually. When, for instance, a small anticyclone is injected, it is accompanied by a domainwide cyclonic "complementary forcing," in the form of a small, spatially constant contribution, additional to (3.1) and spread over the entire domain, such that $\iint F\,dx\,dy$ is zero. That is not to say that the *dynamical* response to a single injection is domainwide. Rather, the complementary forcing is no more than a convenient bookkeeping device to guarantee that the forcing is consistent, at all times, with our choice of model setup including the choice (2.6) and its consequence (2.7).

Consider, for instance, a localized mass injection. The dynamical response is the formation of an anticyclone: namely, a negative anomaly in the q field together with the associated mass and velocity fields obtainable by PV inversion (e.g., Hoskins et al. 1985 and references therein). Those fields describe an outward mass shift and anticyclonically circulating winds, the whole structure extending outward and decaying exponentially on the length scale L_D. The complementary forcing is quite different. It can be pictured as a uniform, domainwide withdrawal of a compensating amount of mass that is small, on the order of the Rossby number, and has no dynamical effect whatever. The complementary forcing

is an artificial device to keep the mass of the model weather layer exactly constant. Of course, with anticyclonic bias, a domainwide mass withdrawal would have to occur in reality, presuming statistical steadiness, and would involve cloud physics and radiative heat transfer (e.g., Li et al. 2006). However, that aspect of the problem is invisible to the quasigeostrophic dynamics.[5]

c. The vortex-injection scheme

We have explored many vortex-injection schemes, with many choices of the way in which injected vortex strengths $|q_{\rm pk}|$ and fractional bias b are made to increase with the interface elevation or coldness ζ. The simplest choices, with strengths increasing monotonically with ζ, produced runaway situations with vortices far stronger than the real planet's mean shears and observed vortices, incompatible with our aim of finding flow regimes that are both realistic and statistically steady.

After much experimentation, the following vortex-injection scheme proved successful, one aspect of which is that $|q_{\rm pk}|$ is never allowed to exceed a set value $q_{\max} > 0$. The sensitivity to interface elevation or coldness is set by a parameter $\psi_{\rm lim} > 0$, in terms of which the definition of ζ will be written as

$$\zeta(x,y,t) = \frac{\widetilde{\psi}_{\rm deep}(y) - \psi(x,y,t)}{\psi_{\rm lim}}, \tag{3.2}$$

where

$$\widetilde{\psi}_{\rm deep}(y) := LU_{\max}\cos\left(\frac{y}{L}\right), \tag{3.3}$$

corresponding to the y-oscillatory or jetlike part of the deep flow (2.3).[6] Injections are done one pair at a time, with the intervening time intervals selected at random from a specified range $[4\Delta t, t_{\max}]$, with uniform probability. The minimum value $4\Delta t$ ensures that injection events do not overlap in time. The maximum value $t_{\max}$ is usually chosen to be much larger, such that $(1/2)t_{\max}$, close to the average time interval, is on the same order as the background shearing time $L/U_{\max}$. We interpret these temporally sparse injections as idealizing the intermittency of the real convection, probably governed by slow but chaotic dry-convective dynamics along with time-variable structure near the interface (e.g., Showman and de Pater 2005; Sugiyama et al. 2014).

For each injection event a location $\mathbf{x} = (x, y)$ is chosen at random and a close-spaced but nonoverlapping pair of vortices, each of radius r_0 as specified in (3.1), is injected at the pair of neighboring points

$$(x_c, y_c) = \left(x \pm \frac{1}{2}s, y\right), \tag{3.4}$$

where the separation s is fixed at

$$s = 2r_0 + \Delta x. \tag{3.5}$$

We denote the respective strengths by $q_{\rm pk} = q_{\rm pkC} > 0$ for the cyclone and $q_{\rm pk} = q_{\rm pkA} < 0$ for the anticyclone, with magnitudes always in the ratio $B \le 1$ where

$$B = \left|\frac{q_{\rm pkC}}{q_{\rm pkA}}\right| = (1-b). \tag{3.6}$$

The fractional bias b is either 1, to give anticyclones only, as in Li et al. (2006) and in Showman (2007), or

$$b = b(\zeta) = b_{\max}\rho(\zeta) \tag{3.7}$$

in all other cases, where $b_{\max} < 1$ is a positive constant and where $\rho(\zeta)$ is the three-piece ramp function defined by

$$\rho(\zeta) := \begin{cases} 0, & \zeta \le -\dfrac{1}{2}, \\ \dfrac{1}{2} + \zeta, & -\dfrac{1}{2} \le \zeta \le \dfrac{1}{2}, \\ 1, & \zeta \ge \dfrac{1}{2}. \end{cases} \tag{3.8}$$

This function is plotted as the top, light-colored curve in the main part of Fig. 2.

It remains to choose how $|q_{\rm pkA}|$ varies. The simplest choice would be

$$|q_{\rm pkA}| = q_{\max}\rho(\zeta), \tag{3.9}$$

implying that $|q_{\rm pkA}|/q_{\max}$ is given by the light-colored curve in Fig. 2. Then $q_{\rm pkC}/q_{\max}$ is given by the curves underneath, for values of $b_{\max} < 1$, plotted using (3.9) with (3.6)–(3.8). The label 1 marks the null curve $q_{\rm pkC}/q_{\max} = 0$ for the anticyclones-only case $b = 1$. However, the choice (3.9) still produces runaway situations incompatible with statistical

[5] A reviewer's comment prompts us to remark that spatially uniform layer-mass changes are invisible to quasigeostrophic *channel* dynamics also. The first equation in (2.6), and the remarks below (2.6), still apply.

[6] Because of its double periodicity, our idealized model has no way of representing large-scale gradients in $\overline{\psi}_{\rm deep}$ except insofar as $d\overline{\psi}_{\rm deep}/dy = -\overline{u}_{\rm deep}$ enters the background PV gradient (2.4). Of course the model also ignores the real planet's other large-scale gradients and associated mean meridional circulations. Examples include large-scale gradients in L_D, in temperature, and in chemical composition including hydrogen ortho–para fraction (e.g., Read et al. 2006, Fig. 10).

steadiness, except when $q_{\max}$ is made too small to produce significant small-scale vortex activity. For larger $q_{\max}$ values, enough to produce such activity, the typical behavior is the growth and unbounded strengthening of a large cyclone. The large cyclone's cold-interface footprint in ζ, still larger in area, induces strong local injections from which the small injected cyclones tend to migrate inward and the small anticyclones outward to give a cumulative, and apparently unbounded, increase in the large cyclone's size and strength. (Notice, by the way, that this mechanism is quite different from the classic vortex merging or upscale energy cascade. The possibility of an unbounded increase in vortex strength is another peculiarity of quasigeostrophic theory, predicting its own breakdown as Rossby numbers increase.)

Large, strong cyclones have correspondingly large q' values, motivating our final choice, which is to use (3.6)–(3.9)—remembering that $q_{\mathrm{pkC}} = B|q_{\mathrm{pkA}}|$—whenever the local q' value satisfies

$$\max(B|q_{\mathrm{pkA}}| + q', |q_{\mathrm{pkA}}| - q') \le q_{\max} \qquad (3.10)$$

whereas, if (3.9) gives a $|q_{\mathrm{pkA}}|$ value that makes the left-hand side of (3.10) greater than $q_{\max}$, then $|q_{\mathrm{pkA}}|$ is reduced just enough to achieve equality, that is, reduced just enough to satisfy (3.10), with B unchanged. The second argument of the max function in (3.10) covers the possibility that strong anticyclones with large negative q' might occur, though it is the first argument that prevails in all the cases we have seen.

The limitations thus placed on the strongest vortices injected are interpreted here as reflecting not only the limitations of quasigeostrophic theory but also the unknown limitations of the real, three-dimensional moist convection as a mechanism for generating coherent vortices on the larger scales represented by our model. On smaller scales, one must expect three-dimensionally turbulent vorticity fields with still stronger peak magnitudes—as terrestrial tornadoes remind us—though, with no solid lower surface, the details are bound to be different. For one thing, net mass injection rates are bound to be modified by such phenomena as evaporation-cooled, precipitation-weighted thunderstorm downdrafts, also called microbursts, contributing negatively. The concluding remarks in section 8 will suggest a possible way of replacing (3.10) by something less artificial, albeit paid for by further expanding the model's parameter space.

d. *Quasi-frictional effects*

As mentioned earlier, the bias b has quasi-frictional effects. These are most obvious in the zonal-mean dynamics described by (2.8) under the constraints (2.5)–(2.7). Because of thermal wind balance and the positive slope of the ramp function $\rho(\zeta)$, the sign of $\overline{F}(y, t)$ tends on average to be anticyclonic in belts and cyclonic in zones whenever the upper or weather-layer jets are stronger than the deep jets [(3.3)], the case sketched in Fig. 1. The converse holds in the opposite case. So $\overline{F}$ tends, on average, to reduce differences between shears in the upper jets and in the deep jets. There is a corresponding quasi-frictional effect on large cyclones. By contrast, fluctuations such as those giving rise to the eddy-flux term $[-\partial(\overline{v'q'})/\partial y]$ in (2.8) can act in the opposite sense, in some cases giving rise to realistic interface-temperature structures in the manner sketched in Fig. 1.

We find that the quasi-frictional effects can be understood alternatively from environment-dependent negative contributions to the right-hand side of the energy equation (2.10), competing with the positive, environment-independent "self energy" inherent in each injection. This contrasts with the standard, perfectly unbiased forcing used in beta-turbulence theory (e.g., Srinivasan and Young 2012), which is designed such that the self-energy is the only contribution, allowing one to prescribe a fixed, positive energy input rate ε, which, along with spectral narrowness, is the normal prelude to using Kolmogorovian arguments. However, it would then be necessary to introduce a separate large-scale dissipation term, as would be necessary also if cyclonic bias, $b < 0$, were to be used in our scheme. (Not surprisingly, taking $b < 0$ has antifrictional effects. When we tried it, the most conspicuous result was self-excitation of unrealistic long-wave undulations.)

When $\overline{F}$ and other quasi-frictional effects with $b > 0$ are strong enough to produce realistic, statistically steady flow regimes, we find that upper-jet profiles tend to be pulled fairly close to deep-jet profiles. This tendency shows up robustly in test runs initialized with upper jets both weaker and stronger than the deep jets. In most cases, therefore, we use a standard initialization in which the upper-jet profiles are the same as the deep-jet profiles (3.3), making $\zeta = 0$ to start with, and the average forcing spatially uniform. We then observe how the upper-jet profiles change in response to the eddy flux $\overline{v'q'}$ in (2.8) and how the ζ and average-forcing fields change in sympathy.

4. Parameter choices

a. *Sensitivity*

It turns out that the interesting cases, statistically steady with realistic, quasi-zonal ζ or interface-temperature structure, occupy only a small region within the model's vast parameter space. Not surprisingly, the behavior is sensitive to $q_{\max}$ and L_D values, which govern the strength

and nature of the model's vortex activity all the way from cases with no such activity—having only the Kelvin/CE2/SSST/ZI passive-shearing mechanism—up to cases with vortex activity so violent as to disrupt the quasi-zonal ζ structure altogether. It turns out that the Kelvin mechanism is unable to produce realistic ζ structure (see section 7 below). The most interesting cases, our main focus, turn out to be those exhibiting chaotic vortex interactions just strong enough to make an impact on the y profiles of $\overline{v'q'}$ in (2.8).

A big surprise, though, was that the behavior is very sensitive to the choice of $b_{\max}$, with the most interesting cases clustered around small values $\lesssim 10^{-1}$. This was especially surprising in view of the past work of Li et al. (2006) and Showman (2007) using purely anticyclonic forcing ($b = 1$). The different behavior seems related in part to the absence of deep jets in their studies but presence in ours. Some further discussion is given in section 6f below.

b. L_D values and A2 stability

In considering choices of L_D, and remembering its latitude dependence, we would like to respect observational as well as theoretical constraints. However, for one thing, observational constraints from the comet-impact waves are controversial and unclear.[7] Also, observational constraints from the DI work and its successors apply mainly to the lower latitudes of the Great Red Spot and other large anticyclonic Ovals, roughly 15°–35°. The original DI work suggested L_D values at, say, 35°S that were not tightly constrained but were estimated as roughly in the range 1500–2250 km. The more recent work of Shetty and Marcus (2010), based on a much more sophisticated cloud wind methodology, appears to constrain L_D values more tightly, for instance producing values close to 1900 km at latitudes around 33.5°S from an analysis of the flow around a large anticyclone, Oval BA. However, unlike DI, who used 1½-layer primitive equation dynamics, Shetty and Marcus (2010) assumed that quasigeostrophic 1½-layer dynamics applies accurately to the real planet. In any case, it is likely that all these estimates apply to the locally deeper weather layer expected near large anticyclones, suggesting somewhat smaller L_D values farther eastward or westward, as well as farther poleward in virtue of the increasing Coriolis parameter.

Our approach will be to reserve judgment on these issues and simply to find a range of L_D values for which the idealized model behavior looks realistic.

As indicated near the end of section 1, we need to keep the model's jets straight by excluding long-wave shear instability. With nonmonotonic upper PV gradients our model has a shear-instability threshold strongly influenced by the value of L_D, as does, almost certainly, the real planet as well. Linear theory shows that, when the threshold is slightly exceeded, the instability first kicks in as a long-wave undulation, phase coherent between adjacent jets, a fact that we have cross-checked in test runs with the unforced model showing, in addition, that the undulation equilibrates nonlinearly to a moderately small amplitude (Thomson 2015, section 4.1) without otherwise disturbing the PV distribution to any significant extent. Such a phase-coherent long-wave undulation would be conspicuous on the real planet but is not observed. To get straight jets, we must stay below the shear-instability threshold.

In our model, for upper-jet profiles kept close to the deep-jet profiles (3.3) by the quasi-frictional $\overline{F}$ effect, the upper-PV gradients are indeed nonmonotonic, and strongly so if we take plausible values of $U_{\max}$ and $\beta - k_D^2 U_0$. Recall (2.3) and (2.4), noting that the y-oscillatory part of the k_D^2 term in (2.4) is small when the upper-jet and deep-jet profiles are close—that is, when $\overline{u}(y)$ is close to $\overline{u}_{\text{deep}}(y) - U_0$.

If, for instance, we take $U_{\max} \simeq 30\,\text{m}\,\text{s}^{-1}$ and $\beta - k_D^2 U_0$ anywhere between the value zero suggested by DI's results and the value of β itself at the equator, about $5 \times 10^{-12}\,\text{s}^{-1}\,\text{m}^{-1}$, then we get strongly nonmonotonic $\partial\overline{q}/\partial y$ essentially because, with $L = (2\pi)^{-1} \times 10\,000\,\text{km} = 1592\,\text{km}$, we have $\partial^2\overline{u}/\partial y^2$ values in the range $\pm U_{\max}/L^2 = \pm 12 \times 10^{-12}\,\text{s}^{-1}\,\text{m}^{-1}$, whose magnitude is well in excess of β at any latitude.

The model's jet flow is then shear unstable for sufficiently large L_D/L but stabilized when L_D/L is taken below the threshold already mentioned, despite the strongly nonmonotonic $\partial\overline{q}/\partial y$. The existence of that threshold was recognized by Ingersoll and Cuong (1981) and, as pointed out by Dowling (1993), is related to the "A2 stabilization" described by Arnol'd's second stability theorem. It arises because reducing L_D/L reduces the intrinsic phase speeds and lateral reach of even the longest, hence fastest possible, pair of counterpropagating Rossby waves, each wave propagating upstream on adjacent prograde and retrograde jets. These reductions suppress the instability by "destroying the ability of the two Rossby waves to keep in step" [McIntyre and Shepherd (1987, p. 543); see also Hoskins et al. (1985,

[7] One reason is that even if the comet-impact waves were gravity waves guided by the weather layer they would have had a different structure in the underlying dry-convective layer, more like surface–gravity wave structure than that of 1½-layer dynamics. Another reason is the case made by Walterscheid (2000) that the observed comet-impact waves were in any case more concentrated in Jupiter's stratosphere.

Fig. 18ff., and references therein)]—that is, to phase lock, with each wave holding its own against the mean flow. That is why the first wavelength to go unstable for slightly supermarginal L_D/L is the *longest* available wavelength, with zonal wavenumber $k_{\min}$, say.

For unbounded or doubly periodic domains the A2 theorem says that the flow is shear stable if a constant c can be found such that

$$k_D^2 + k_{\min}^2 > \frac{\partial \overline{q}/\partial y}{\overline{u} - c}, \tag{4.1}$$

where as before $k_D^2 := L_D^{-2}$. For the sinusoidal profiles of our standard initialization, and for $\beta - k_D^2 U_0 = 0$ as suggested by DI, it happens that (4.1), with $c = 0$, is a necessary as well as a sufficient condition for stability (Stamp and Dowling 1993). The right-hand side of (4.1) is then just L^{-2}, independent of $U_{\max}$, and the threshold is precisely at $k_D^2 = L^{-2} - k_{\min}^2$.

In our model, with its 2:1 aspect ratio, we have $k_{\min}^2 = L^{-2}/4$. Therefore, $L_D \lesssim (4/3)^{1/2} L = 1838$ km should be enough to exclude long-wave shear instability, as long as the upper-jet profiles stay close to the deep-jet profiles. It is arguable, however, that since the much larger domain of the real planet should correspond to $k_{\min}^2 \ll L^{-2}$, it might be more appropriate to take $L_D \lesssim L = 1592$ km. Having regard to these considerations, we decided to use L_D values of 1500 km or less in most of our model runs. In any case it turned out that for larger L_D the typical result was unrealistically strong, or even violent, long-wave disturbances.

In sections 5 and 6 we describe and illustrate the model's behavior for $L_D = 1200$ and 1500 km and for forcings just strong enough to produce chaotic vortex interactions. In such cases the model robustly approaches stable, statistically steady states with fairly straight jets, and realistic ζ structures, over significant ranges of $q_{\max}$ and $b_{\max}$ and with nonmonotonic upper PV gradients $\partial \overline{q}/\partial y$.

c. *Other parameters including β_0 and $q^*_{\max}$*

We fix $U_{\max} = 35\ \mathrm{m\,s^{-1}}$ as a compromise between low- and midlatitude values, and choose two values of

$$\beta_0 := \beta - k_D^2 U_0; \tag{4.2}$$

namely, zero and $4.03 \times 10^{-12}\ \mathrm{s^{-1}\,m^{-1}}$. Both choices make $\partial \overline{q}/\partial y$ strongly nonmonotonic. The value zero requires prograde U_0, roughly consistent with DI's results; see DI's Fig. 4b and its idealization in Stamp and Dowling (1993). Prograde U_0 is in any case expected in latitudes outside a tangent cylinder of the dry-convective layer (e.g., Jones and Kuzanyan 2009). The value $4.03 \times 10^{-12}\ \mathrm{s^{-1}\,m^{-1}}$ is the value of β itself at latitude 35°. For convenience, we refer to these two cases $\beta_0 = 0$ and $\beta_0 = 4.03 \times 10^{-12}\ \mathrm{s^{-1}\,m^{-1}}$ as "pure DI" and "midlatitude," respectively, remembering, however, that nothing is known observationally about actual U_0 values at the higher latitudes.

Because the quasi-frictional $\overline{F}$ effect tends to pull our model's upper jets more or less close to its deep jets, the strongest upper mean shears $\partial \overline{u}/\partial y$ tend to have orders of magnitude similar to that of the strongest deep shear $U_{\max}/L = 2.199 \times 10^{-5}\ \mathrm{s^{-1}}$. So a convenient dimensionless measure of $q_{\max}$ is

$$q^*_{\max} := \frac{q_{\max}}{U_{\max}/L} > 0. \tag{4.3}$$

The parameter $q^*_{\max}$ governs the likely fate of vortices injected into background shear of order $U_{\max}/L$. We take values ranging from $q^*_{\max} = 0.5$ up to $q^*_{\max} = 32$. At the low end of the range, practically all the injected vortices are shredded (i.e., sheared passively and destroyed). (There is still, of course, a quasi-frictional $\overline{F}$ effect.) In the highest part of the range, say $16 \lesssim q^*_{\max} \lesssim 32$, the strongest injected vortices all survive even in adverse shear (e.g., anticyclones in cyclonic shear). For intermediate values one typically sees survival in favorable shear only. To distinguish the three types of behavior we call the injections "weak," "strong," and "semistrong," respectively.

The behavior is roughly consistent with the classic study of Kida (1981) on single vortices in shear. In place of the parabolic profile $\Delta q(r)$ defined by (3.1) above, Kida's analysis assumes that $L_D = \infty$ and uses a top hat or "vortex patch" profile. It should be qualitatively relevant for small vortex radius $r_0 \ll L_D$. Kida's condition for an anticyclone of strength q_{patch} to survive in cyclonic shear S is $q^*_{\mathrm{patch}} > 6.72$, where $q^*_{\mathrm{patch}} := |q_{\mathrm{patch}}/S|$, as can be shown straightforwardly from his equations.[8]

[8] The number 6.72 can be verified from the first line of Kida's (3.4) by setting $s = 1$ and plotting the right-hand side over an interval $r \in (0, 1)$. In Kida's notation $r = 1$ corresponds to a circular vortex and $r = 0$ corresponds to a vortex shredded by the shear into an infinitely thin filament. Taking $s = 1$ picks out the case of an initially circular vortex. The vortex is shredded if, for all r, the right-hand side of Kida's (3.4) stays between -1 and $+1$, while if it dips below -1 the vortex survives. For adverse pure shear, such a dip occurs whenever, in Kida's notation, $\omega/2e = -\omega/2\gamma > 6.7215$, where $\omega = q_{\mathrm{patch}} < 0$ and $2\gamma = S > 0$, the shear. For favorable pure shear, there is no sharp threshold, but, for instance, favorable pure shear with $0 < -\omega/2e = \omega/2\gamma < 0.5$ distorts an initially circular vortex beyond aspect ratio 25. Its destruction is then a practical certainty for finite L_D or for almost any background differing from Kida's strictly steady, strictly constant pure shear of infinite spatial extent.

Model test runs with single-vortex injections and vortex-pair injections (Thomson 2015, Figs. B10 and B11, respectively) behave as expected from Kida's analysis. For instance, a single parabolic anticyclone of peak strength $|q_{\mathrm{pkA}}|$ injected into cyclonic shear S is destroyed when $|q_{\mathrm{pkA}}/S| \lesssim 7$. It survives almost intact when $|q_{\mathrm{pkA}}/S| \gtrsim 16$, then behaving almost like Kida's patch with the same Kelvin circulation (i.e., with the same value of $2\pi\int_0^{r_0}\Delta q r\,dr$ so that $|q_{\mathrm{patch}}| = (1/2)|q_{\mathrm{pkA}}|$). For intermediate values, $8 \lesssim |q_{\mathrm{pkA}}/S| \lesssim 16$, a small core survives while the outskirts are eroded away.

The parameter ψ_{lim} in (3.2) has to be chosen empirically. We want the resulting ζ fields to range over values within, or slightly exceeding, the range $-1/2 \le \zeta \le +1/2$ that corresponds to the sloping part of the ramp function $\rho(\zeta)$. A satisfactory choice is found to be $\psi_{\mathrm{lim}} = \Lambda q^*_{\mathrm{max}}$ where $\Lambda = 4.47 \times 10^6\ \mathrm{m^2\ s^{-1}}$. This is used in all the runs mentioned here, all the way from $q^*_{\mathrm{max}} = 0.5$ to $q^*_{\mathrm{max}} = 32$. The precise value of Λ is not critical. Any neighboring value will produce similar results.

Table 1 and its caption summarize the parameter choices for the most important runs, labeled as in the first column, with "DI" denoting pure-DI runs and "ML" denoting midlatitude runs, corresponding to the β_0 values shown in column 2. See text following (4.2). The numbers within each label DI-12–16–1, etc., are shorthand for L_D, q^*_{max}, and bias, respectively, as shown also in columns 3–5. Thus, for instance, DI-12–16–1 labels a pure-DI run in which $L_D = 1200$ km, $q^*_{\mathrm{max}} = 16$, and bias $b = 1$ (i.e., anticyclones-only forcing). When the final number exceeds 1, as in runs DI-12–16–4 to DI-12–16–∞, it is the reciprocal of b_{max} in (3.7). In the column marked "Statistically steady?", the blank entries signify runs not yet steady but likely to have become so, in our judgment, had the run been continued for long enough.

5. Main results

a. *Pure-DI with $L_D = 1200$ km, $q^*_{\mathrm{max}} = 16$, and varying bias*

We focus at first on the pure-DI case with $L_D = 1200$ km and $q^*_{\mathrm{max}} = 16$, then comment briefly on similarities and differences for $L_D = 1500$ km and for midlatitude cases. Further details are given in Thomson (2015). It is for $L_D = 1200$ km, well below the A2 stability threshold, that we obtain the widest ranges of q^*_{max} and b_{max} over which model flows are realistic and statistically steady. Broadly speaking, the range of q^*_{max} values that produce such flows is found to be in or near the semistrong regime.

Figures 3–7 show results for the first seven runs in Table 1, in which bias is varied in the pure-DI case with $L_D = 1200$ km and $q^*_{\mathrm{max}} = 16$.

In Fig. 3 the inner, dashed curve is the deep-jet velocity profile $\overline{u}_{\mathrm{deep}}(y) - U_0$. The solid curves are upper-jet profiles $\overline{u}(y)$ for the different biases after 120 yr (Earth years) of integration from the standard initialization. The model belt lies approximately in the y interval between 2500 and 7500 km, where the mean shears are cyclonic, corresponding to the central portion of Fig. 3, and of Fig. 1 also. The model zone is in the periphery and its periodic extension. The upper-jet profiles $\overline{u}(y)$ begin with the anticyclones-only run, DI-12–16–1, which has $b = 1$ for all ζ. This is the first solid curve, thicker than the rest and only slightly different from the dashed curve. The lighter solid curves, peaking at successively higher values of $|\overline{u}|$, correspond to runs DI-12–16–4 to DI-12–16–∞ (i.e., $b_{\mathrm{max}} = 1/4$, 1/8, 1/16, 1/32, 1/64, and 0, respectively). We also ran $b_{\mathrm{max}} = 1/2$; the profile, not shown, hardly differs from the dashed curve and the thick, $b = 1$ profile.

Evidently the actual mean shears in the model belt are either close to, or somewhat greater in magnitude than, the nominal value U_{max}/L in (4.3). Many of the injections in these runs are semistrong, depending on injection locations. A small minority can be strong. The varying behavior of the injections is further discussed below, in connection with an illustrative movie.

As anticipated, reducing the bias reduces the quasi-frictional $\overline{F}$ effect, allowing stronger upper jets. In these pure-DI runs there is no dynamical difference between prograde and retrograde jets, which on average are sharpened and strengthened by the same amounts.

The runs with b_{max} ranging from 1/4 to 1/16, and the run with $b = 1$, are all close to statistical steadiness, consistent with the flattening out of the corresponding curves in Fig. 4. These give domain-averaged total energy ($\mathrm{J\,kg^{-1}}$) against time t, with bias decreasing upward from curve to curve. Total energies are dominated by $(1/2)|\overline{u}|^2 + (1/2)k_D^2|\overline{\psi}|^2$, the kinetic plus available potential energy of the zonal-mean flow, contributing in roughly equal proportions. Domain-averaged eddy energies (not shown) are relatively small but also flatten out, for the runs in question. The run with $b_{\mathrm{max}} = 1/32$ corresponds to the topmost of the three energy curves that reach 250 yr. It is evolving toward statistical steadiness but does not come close to it until something like 500 yr of integration. The run with $b = 1$, included for comparison and contrast with Li et al. (2006) and Showman (2007), is statistically steady apart from a decadal-time-scale vacillation (thick curve at bottom of Fig. 4). However, in that run the upper jets are hardly stronger than the deep jets, as seen in Fig. 3, and the ζ structure is correspondingly unrealistic.

TABLE 1. Parameter values chosen. In column 5, the bias values are $b = 1$ or $b_{max} < 1$; see text surrounding (3.7). The t_{run} column shows the length of each run, rounded down to the nearest 5 Earth years. Statistical steadiness (column 7) is assessed at $t = t_{run}$. The blank entries (—) signify runs not yet steady but judged likely to become so. The parameter ψ_{lim} defined in (3.2) is set equal to Λq^*_{max} where $\Lambda = 4.47 \times 10^6\ m^2\ s^{-1}$; Λ is always held fixed. Also, t_{max}, defined below (3.3), is 24.06 h in all runs except the last two (DI-12–1–64 and DI-12–0.5–64), for which $t_{max} = 0.2406$ h. Other parameters held fixed are $U_{max} = 35\ m\ s^{-1}$, $L = 1591.55$ km, $r_0 = 156.25$ km, $\Delta x = \Delta y = 39.0625$ km, $\Delta t = 50$ s, $U_{max}/L = 2.199 \times 10^{-5}\ s^{-1}$, and the injected-vortex separation $s = 2r_0 + \Delta x = 351.56$ km [see (3.5)]. However, Δx, Δy, and Δt are halved in numerical resolution tests, as described in Thomson (2015, section 3.5.2).

Run	β_0 [$s^{-1}m^{-1}$; (4.2)ff.]	L_D [km; (2.2)ff.]	q^*_{max} [(4.3)]	Bias [(3.6)ff.]	t_{run} (yr)	Statistically steady?	Figures
DI-12–16–1	0	1200	16	1	125	Yes	Figs. 3, 4, 6, 7
DI-12–16–4	0	1200	16	1/4	125	Yes	Figs. 3, 4, 6, 7
DI-12–16–8	0	1200	16	1/8	250	Yes	Figs. 3, 4, 6, 7
DI-12–16–16	0	1200	16	1/16	710	Yes	Figs. 3–7
DI-12–16–32	0	1200	16	1/32	710	Yes	Figs. 3, 4, 6, 7
DI-12–16–64	0	1200	16	1/64	125	No	Figs. 3, 4, 6, 7
DI-12–16–∞	0	1200	16	0	125	No	Figs. 3, 4, 6, 7
ML-12–16–1	4.03×10^{-12}	1200	16	1	125	Yes	Figs. 8, 9
ML-12–16–4	4.03×10^{-12}	1200	16	1/4	125	Yes	Figs. 8, 9
ML-12–16–8	4.03×10^{-12}	1200	16	1/8	250	Yes	Figs. 8, 9
ML-12–16–16	4.03×10^{-12}	1200	16	1/16	290	Yes	Figs. 8, 9
ML-12–16–32	4.03×10^{-12}	1200	16	1/32	240	—	Figs. 8, 9
ML-12–16–64	4.03×10^{-12}	1200	16	1/64	125	No	Figs. 8, 9
ML-12–16–∞	4.03×10^{-12}	1200	16	0	125	No	Figs. 8, 9
DI-15–16–16	0	1500	16	1/16	295	Yes	Thomson (2015)
ML-15–16–16	4.03×10^{-12}	1500	16	1/16	60	—	Thomson (2015)
DI-15–8–8	0	1500	8	1/8	60	—	Thomson (2015)
DI-15–8–16	0	1500	8	1/16	320	Yes	Thomson (2015)
ML-15–8–8	4.03×10^{-12}	1500	8	1/8	60	—	Thomson (2015)
ML-15–8–16	4.03×10^{-12}	1500	8	1/16	315	Yes	Thomson (2015)
DI-12–8–16	0	1200	8	1/16	125	—	Thomson (2015)
ML-12–8–16	4.03×10^{-12}	1200	8	1/16	110	—	Thomson (2015)
DI-12–32–16	0	1200	32	1/16	330	Yes	Thomson (2015)
DI-12–1–16	0	1200	1	1/16	350	—	Thomson (2015)
DI-12–1–64	0	1200	1	1/64	300	Yes	Figs. 10–13
DI-12–0.5–64	0	1200	0.5	1/64	300	Yes	Figs. 10–13

b. *Details and movie for a realistic example*

We focus on run DI-12–16–16. Figure 5 shows snapshots of ζ in contours and q in grayscale for that run, at time $t = 120$ yr. A corresponding q-field movie is provided in the online supplemental material, in grayscale and color versions. The bars on the right show L_D. Solid contours in Fig. 5a show positive ζ, a cold, elevated interface that increases moist-convective activity. The thick solid contour marks the value $\zeta = +1/2$ at which the ramp function $\rho(\zeta)$ saturates. Dashed contours show negative ζ, a warm, depressed interface that reduces moist-convective activity. The structure of this ζ field is sufficiently zonal to count as realistic, by our criterion that the model should reflect the real planet's preference for stronger convection in belts than in zones.

The q snapshot in Fig. 5b is dominated by small vortices, produced by injections followed by migration—especially of small anticyclones from the belt into the zone—as well as by occasional vortex merging and other interactions. Cyclones are shown dark and anticyclones are shown light. The small vortices move around chaotically under their neighbors' influence and that of the background shear. Yet vortex merging and upscale energy cascading are inhibited to a surprising extent. This lack of upscale cascading will be discussed further in section 6.

Conspicuous in Fig. 5b is a single, relatively large cyclone near $x \simeq 7500$ km and $y \simeq 5000$ km. The strength of this cyclone fluctuates but is statistically steady. The snapshot shows it slightly larger and stronger than average. The strength is governed by reinforcement mainly through local injections and internal migration on the one hand (section 6b below), competing with attrition by erosion and quasi-frictional effects on the other. The cyclone is strong enough to produce a conspicuous footprint in the ζ field, superposed on the quasi-zonal structure (Fig. 5a). The footprint takes the form of a cold patch or elevated area

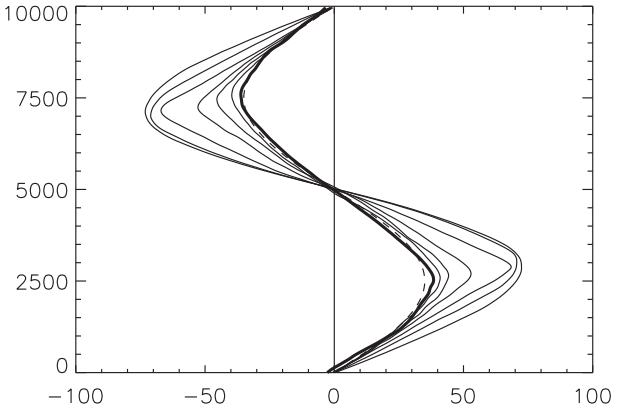

FIG. 3. Zonal-mean zonal velocity profiles $\overline{u}(y)$ (m s^{-1}; y axis in kilometers) for the pure-DI case with $L_D = 1200$ km and $q^*_{\max} = 16$, all shown at time $t = 120$ Earth years. The inner, dashed curve is $\overline{u}_{\text{deep}}(y) - U_0$. The thick solid curve is the upper profile $\overline{u}(y)$ for the anticyclones-only run, $b = 1$ for all ζ (run DI-12–16–1). The lighter solid curves show $\overline{u}(y)$, in order of increasing peak $|\overline{u}|$, respectively, for $b_{\max} = 1/4, 1/8, 1/16, 1/32, 1/64$, and 0 (runs DI-12–16–4, DI-12–16–8, . . . , DI-12–16–∞).

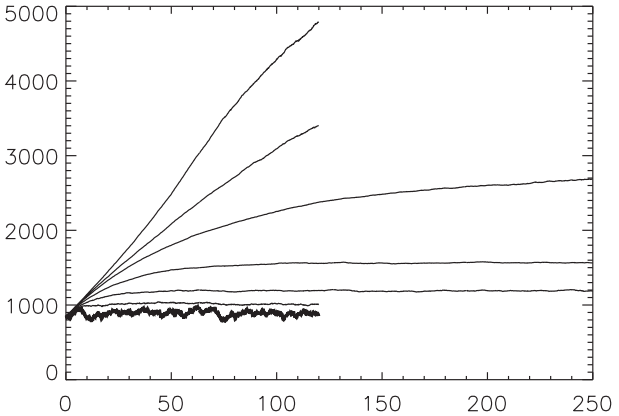

FIG. 4. Domain-averaged total energy per unit mass (J kg^{-1} or m^2 s^{-2}) against time (Earth years) for the same set of pure-DI runs as in Fig. 3, with $L_D = 1200$ km and $q^*_{\max} = 16$. The lowest, thick solid curve is for the anticyclones-only run, $b = 1$ for all ζ. The lighter solid curves, reaching successively higher energies, correspond, respectively, to $b_{\max} = 1/4, 1/8, 1/16, 1/32, 1/64$, and 0.

extending outward from the core of the cyclone on the length scale L_D.

The velocity field of the large cyclone modifies the background shear and strain quite substantially, such that some of the nearby injection events are strong rather than semistrong. An example can be seen in the movie, starting west-southwest of the large cyclone at $t_{\text{rel}} = 0.408$, where time t_{rel} runs from 0 to 1 in units of movie duration, just under an Earth month. The injected anticyclone survives as it travels around the large cyclone, protected by the cyclone's *anticyclonic* angular shear, then slowly migrates into the model zone to the north, across the retrograde jet. The accompanying cyclone, caught in the same anticyclonic angular-shear environment, suffers partial erosion almost immediately after injection. It has a much shorter lifetime and ends up completely shredded, at $t_{\text{rel}} \simeq 0.58$, after one more partial erosion event.

Another clear example of migration from belt to zone, this time southward, occurs between $t_{\text{rel}} \simeq 0.65$ and $t_{\text{rel}} \simeq 0.9$. A recently injected anticyclone partly merges with a preexisting anticyclone, near $x \simeq 15\,000$ km and $y \simeq 3000$ km, and then migrates from belt to zone across the southern, prograde jet.

The snapshot in Fig. 5b is taken at the start of the movie, $t_{\text{rel}} = 0$. At that instant, there has just been an injection almost due west of the large cyclone, near $x \simeq 5000$ km. That injection proves to be semistrong. Its anticyclone, seen on the left in Fig. 5b, is shredded immediately. However, its cyclone is also shredded shortly afterward, again by the anticyclonic angular-shear environment. During this cyclone's short lifetime ($t_{\text{rel}} \lesssim 0.13$), it migrates inward through a small radial distance, as can be checked by comparing its positions south and then north of the large cyclone, at $t_{\text{rel}} = 0.040$ and 0.098, respectively. Such events are frequent and are clearly part of what builds the large cyclone, whose typical q structure is sombrero-like, a strong cyclonic core surrounded by a weaker, fluctuating cyclonic region, easier to see in the color movie than in the gray-scale snapshot. That structure is alternately built up and eroded by a chaotic sequence of vortex interactions and injections.

Also notable in the movie is an injection making a rare direct hit on the inner core of the large cyclone at $t_{\text{rel}} = 0.044$. Thanks to the condition (3.10), this injection behaves as a semistrong injection. In this case the injected anticyclone is shredded into a tight spiral and acts quasi frictionally. By contrast, the injected cyclone stays almost completely intact and migrates through a small radial distance to the center. The net effect is a slight reduction in the overall size and strength of the large cyclone, from above average to below average.

c. *Varying bias again*

Most of the statistically steady runs produce a single, relatively large cyclone in a similar way. Its average size increases as $b_{\max}$, hence quasi-frictional effects, are reduced. Runs DI-12–16–64 and DI-12–16–∞, with $b_{\max} = 1/64$ and 0, were terminated at $t = 125$ yr because by then they had developed single cyclones large enough to produce an unrealistic, grossly nonzonal, footprint-dominated ζ structure.

The sharpened peaks of the jet profiles for $b_{\max} = 1/16$ in Fig. 3 correspond to sharp steps in the q field, as seen

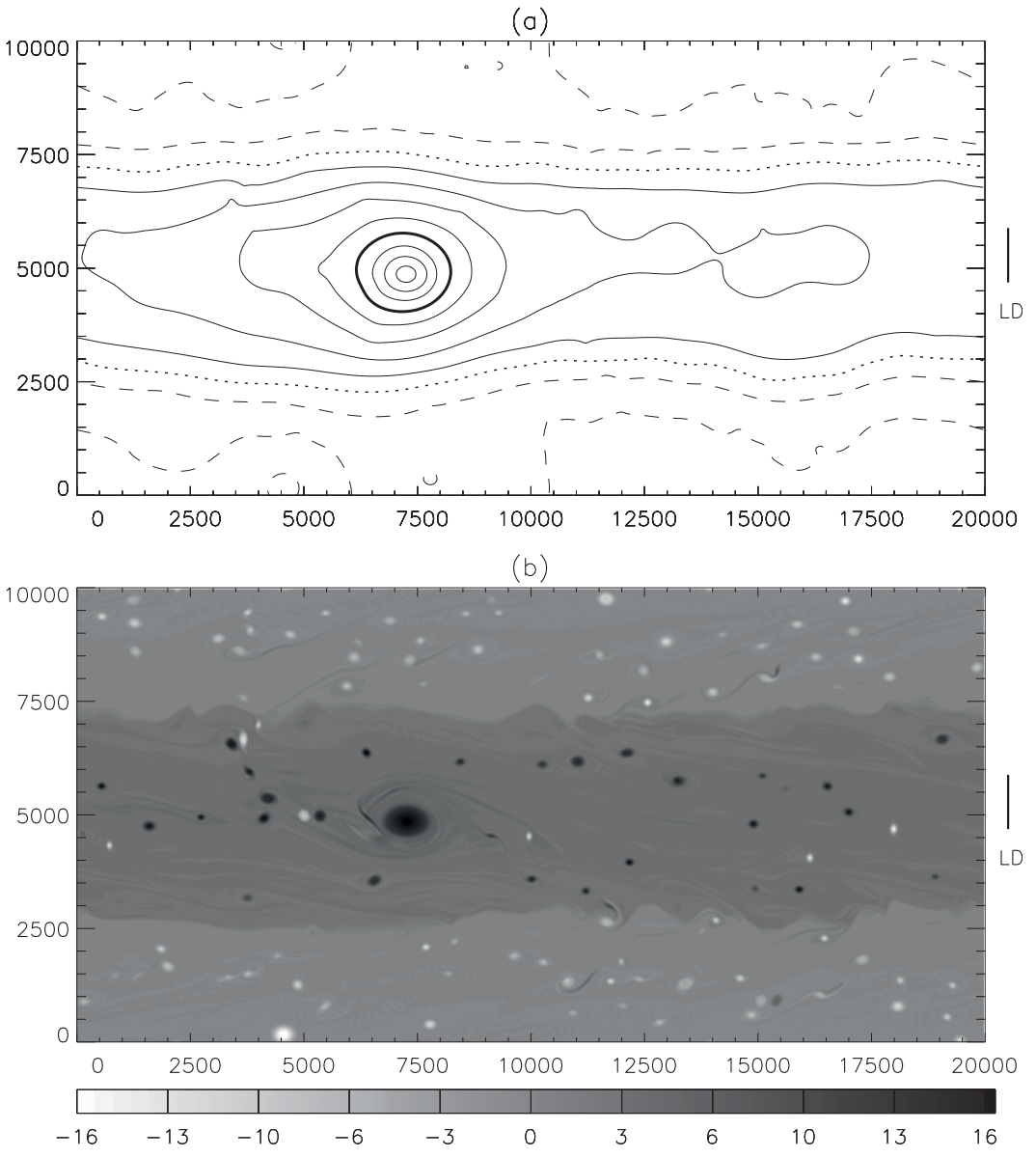

FIG. 5. Snapshots of the ζ and q fields at time $t = 120$ Earth years for run DI-12–16–16 (x and y axes in kilometers). (a) Dashed contours show negative ζ and solid contours show positive ζ, with a contour interval of 0.1 in the dimensionless units of Fig. 2. The thick solid contour marks the value $\zeta = +0.5$ at which the ramp function $\rho(\zeta)$ saturates. (b) The grayscale is in units of $U_{\max}/L = 2.199 \times 10^{-5}\ \mathrm{s}^{-1}$, like $q^*_{\max}$. The strongest vortices slightly exceed the grayscale range, with the large cyclone in midbelt, $y \simeq 5000$ km, peaking at $q = 17.8U_{\max}/L$, and the largest anticyclone, to the far south-southwest of it, near $x \simeq 4500$ km, peaking at $q = -18.4U_{\max}/L$. There is one other out-of-range vortex, the small cyclone north-northwest of the large cyclone, near $x \simeq y \simeq 6400$ km, which peaks at $q = 17.7U_{\max}/L$.

in Fig. 5b as sharp transitions between light gray and darker gray. These PV steps, embedded as they are in relatively uniform surroundings, resemble the cores of terrestrial strong jets apart from their relatively limited meandering, which is much more Jupiter-like. The formation of such steps from an initially smooth q field points to PV mixing across belts and zones as a contributing mechanism. A role for PV mixing is consistent with the chaotic appearance of the small-scale vortex interactions.

The PV steps persist into the two regimes with the smallest $b_{\max}$ values 1/64 and 0 and the largest cyclones. However, the PV steps are no longer reflected in the corresponding $\overline{u}(y)$ profiles in Fig. 3, the outermost two

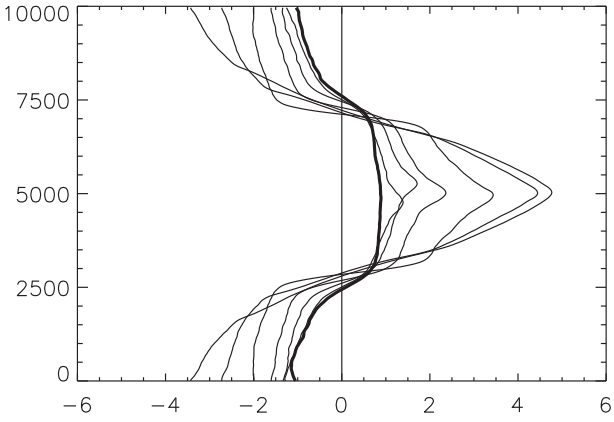

FIG. 6. Zonal-mean PV profiles $\overline{q}(y)$ (y axis in kilometers) for the same set of pure-DI runs as in Fig. 3, with $L_D = 1200$ km and $q^*_{\max} = 16$. The PV is in units of $U_{\max}/L = 2.199 \times 10^{-5}\ \mathrm{s}^{-1}$ and is time averaged from $t = 115$ to $t = 125$ yr to reduce fluctuations. The thick curve is the $\overline{q}(y)$ profile for the anticyclones-only run, $b = 1$ for all ζ, and the lighter curves with increasingly large peak $|\overline{q}|$ values correspond, respectively, to $b_{\max} = 1/4$, $1/8$, $1/16$, $1/32$, $1/64$, and 0. The initial profile (not shown) is sinusoidal with amplitude 1 unit, its central peak only just beyond the flat part of the $b = 1$ thick curve.

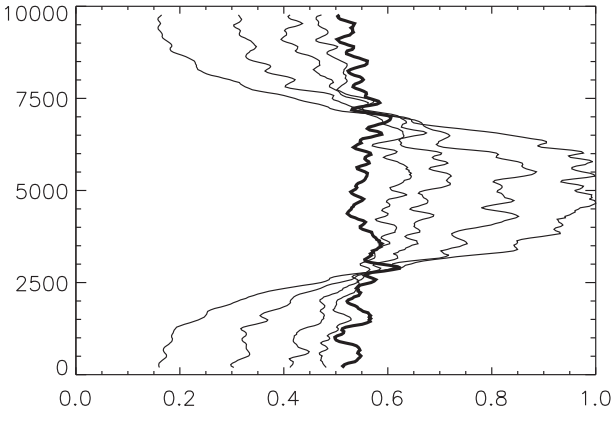

FIG. 7. Relative moist-convective activity $A(y)/A_{\max}$ (y axis in kilometers) for the same set of pure-DI runs as in Fig. 3, except that $b_{\max} = 1/64$ and $b_{\max} = 0$ are omitted. Here $A(y)$ is defined in (5.1), and $A_{\max}$ is the largest value in the set shown. The thick curve is for the anticyclones-only run $b = 1$. The lighter curves are for $b_{\max} = 1/4$, $1/8$, $1/16$, and $1/32$, peaking successively farther to the right. The small wiggles arise from the statistical fluctuations in the vortex-injection scheme, showing up despite time averaging from 60 to 120 yr.

profiles. Being Eulerian means, they are more rounded simply because the large cyclones make the jets meander more strongly. A Lagrangian mean (not shown) would follow the meandering and still reveal sharpened jet profiles—indeed even sharper than the sharpest in Fig. 3.

Figure 6 shows the Eulerian-mean $\overline{q}$ profiles for the same set of pure-DI runs, at time $t \simeq 120$ yr (see caption). For $b_{\max} \geq 1/16$, the profiles reflect the same inhomogeneous-PV-mixing structure, though the large cyclone in Fig. 5b creates a noticeable blip near $y \simeq 5000$ km in the $\overline{q}$ profile for $b_{\max} = 1/16$. Similar blips, corresponding to larger cyclones, become strong and then dominant as $b_{\max}$ is reduced to 1/32, 1/64, and 0; and the large cyclones are still growing in those runs. It is interesting to see what look like hints of PV mixing even for $b = 1$ (thick curve), although the departure from the initial, sinusoidal $\overline{q}(y)$ profile is then very weak (see figure caption) and unable to produce a realistic ζ field.

Figure 7 gives an alternative view of the model's belt–zone structure for $b_{\max} \geq 1/32$. It shows in arbitrary units a positive-definite measure A of average injection strength, defined by

$$A(y) = \overline{|\Delta q(r)|}^{xt} \tag{5.1}$$

where the averaging is over many injections, both zonally and in time. In Fig. 7 the time averaging is from 60 to 120 yr. Here $\Delta q(r)$ represents the cores of injected anticyclones only, as defined in (3.1), omitting their cyclonic companions and complementary forcings. Thus, $A = 0$ would signal a complete absence of injections. Increasing values of A signal increasingly strong injections, on average, regardless of bias. The wiggles in the curves arise from the statistical fluctuations in the vortex-injection scheme.

The belt–zone variation in injection strength seen in Fig. 7 is consistent with the realistic ζ structures found for moderately small values of $b_{\max}$, with the strongest injections concentrated in midbelt. The unrealistic ζ structure for $b = 1$ produces, as expected, relatively little belt–zone variation in injection strength (thick curve). The belt–zone variation increases as $b_{\max}$ decreases toward 1/32 but then decreases again (not shown) because of the dominance of the large cyclone, within whose footprint the condition (3.10) weakens the injections.

d. Other cases and parameter values

Results for $q^*_{\max} = 8$ (not shown; see Thomson 2015) show similar behavior, though the tendency to form large cyclones is weaker, and there are cases in which the largest cyclones come in pairs. Most injections are then weak or semistrong. For $q^*_{\max} = 32$, by contrast, many injections are strong, resulting in relatively violent vortex activity. A long run, DI-12–32–16, has been carried out for $q^*_{\max} = 32$ and $b_{\max} = 1/16$. It shows an unrealistic, strongly nonzonal ζ structure, briefly described in section 6e. For $q^*_{\max} = 1$ or less, practically all injections are weak. The response is then governed mainly by the Kelvin and $\overline{F}$ mechanisms. See section 7.

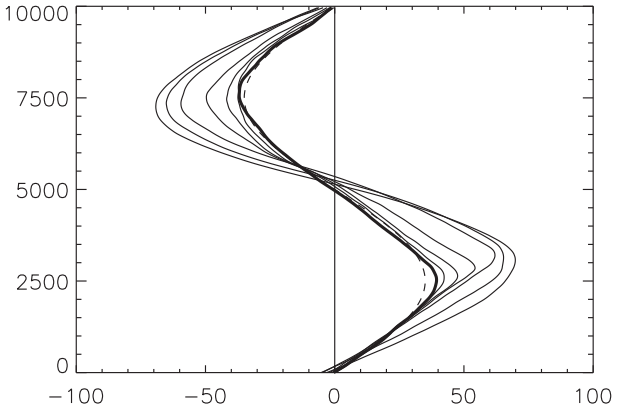

FIG. 8. Zonal-mean zonal velocity profiles $\overline{u}(y)$ (m s^{-1}; y axis in kilometers) for the midlatitude case with $L_D = 1200$ km and $q^*_{\max} = 16$, at time $t = 120$ Earth years. Note that *all* the retrograde jet profiles are rounded. Biases vary as in Fig. 3. These are the runs labeled ML-12–16–1, ML-12–16–4, . . . , ML-12–16–∞.

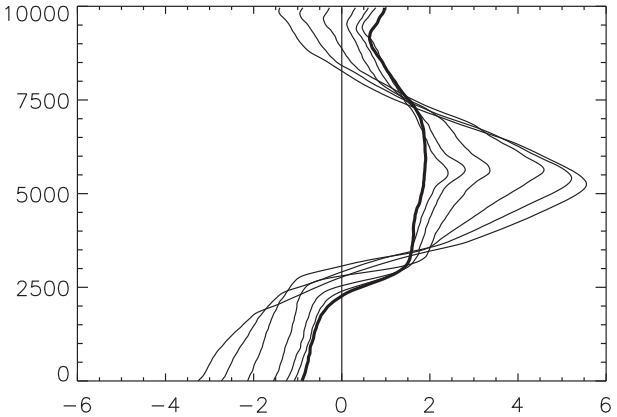

FIG. 9. Zonal-mean PV profiles $\overline{q}(y)$ (y axis in kilometers) for the same set of midlatitude runs as in Fig. 8, with $L_D = 1200$ km and $q^*_{\max} = 16$. The PV is in units of $U_{\max}/L = 2.199 \times 10^{-5}$ s^{-1} and is time averaged from $t = 115$ to 125 yr to reduce fluctuations. Biases vary as in Fig. 6. The background PV gradient (4.03×10^{-12} s^{-1} m^{-1}) makes each profile shear over, with a total displacement of 1.83 units (4.03×10^{-12} s^{-1} m^{-1} $\times 10^{7}$ m $\div 2.199 \times 10^{-5}$ s^{-1} = 1.83).

For the midlatitude case, with $\beta_0 = \beta - k_D^2 U_0 = 4.03 \times 10^{-12}$ s^{-1} m^{-1} (the value of β itself at latitude 35°), the results (Thomson 2015) are broadly similar except that jet sharpening is more effective for the prograde than for the retrograde jets. The $\overline{u}$ and $\overline{q}$ profiles for $L_D = 1200$ km and $q^*_{\max} = 16$ at time $t \simeq 120$ yr are shown in Figs. 8 and 9 (see captions). Again, only the runs with $b = 1$ or $b_{\max} \geq 1/16$ are close to statistical steadiness at $t \simeq 120$ yr.

Notice from Fig. 9 that the $\overline{q}$ profiles are still strongly nonmonotonic. The ζ and q fields for $b_{\max} = 1/16$ are similar to those in Fig. 5, except that the PV step near $y = 7500$ km is distinctly weaker and the large cyclone is distinctly stronger. Concomitantly, the ζ field is somewhat less zonal, with a stronger and larger cyclonic footprint.

The pattern of results for $L_D = 1500$ km is again broadly similar, except that realistic quasi-zonal structure is more easily disrupted. Vortex interactions reach across somewhat greater distances, and the whole system is somewhat closer to the A2 marginal stability threshold. This makes the upper jets more liable to large-scale meandering. The most realistic ζ fields are obtained for a narrower range of $q^*_{\max}$ values, closer to 8 than 16. For further detail, see Thomson (2015).

e. *Regarding statistical steadiness*

As an extreme test of statistical steadiness, we ran our main case DI-12–16–16 out to $t = 710$ yr and compared details at later times with the 120-yr results shown above. All the mean profiles remain nearly indistinguishable from those in Figs. 3, 6, and 7. The q fields are qualitatively indistinguishable from Fig. 5b. In particular, the largest cyclone and anticyclone have similar sizes. By way of illustration a snapshot of the q field at 600 yr is shown in Fig. 4.10 of Thomson (2015).

As a further check, we produced a time series of domain-maximum cyclone strength over the whole time interval from $t = 0$ to 710 yr. The time series showed fairly strong fluctuations, mostly with maximum q values in the range 15–20 in units of $U_{\max}/L$. Many of these fluctuations are fleeting and are, we think, due to transient Gibbs fringes produced by the high-wavenumber filter, during interactions involving the strongest small cyclones. The main point, however, is that even this sensitive time series looks statistically steady from $t \simeq 100$ yr onward, all the way out to $t = 710$ yr.

6. Mechanisms in play

a. *To merge or not to merge*

Repeated vortex merging, giving rise to an upscale energy cascade as vortices get larger—a stepwise energy transfer in wavenumber space—is often taken for granted as an essential mechanism in all two-dimensionally turbulent flows. It therefore came as a surprise to us to discover that the cascade mechanism plays no significant role at all in our most realistic cases.

In these cases the stochastic forcing is strong enough to produce nonlinear behavior in the form of chaotic vortex interactions. The vortices follow trajectories resembling random walks, encountering each other in a quasi-random way, as is evident from q-field movies such as that discussed in section 5b. Vortex-merging events do occur, as noted in that discussion, but require

extremely close encounters and are much rarer than vortex-erosion events. Except for one or two large cyclones, such as the single large cyclone in Fig. 5b, all the other vortices remain small in all the realistic cases we have seen—in order-of-magnitude terms, not much larger than the vortices originally injected. The largest anticyclone in Fig. 5b, at the bottom of the figure near $x \simeq 4500$ km, shows that whatever merging events took place during the preceding 120 yr, they could not have been enough to produce much systematic growth in vortex size despite the favorable background shear.[9]

A contributing factor is the sparseness of our vortex injection scheme, idealizing the intermittency of real Jovian moist convection as in Li et al. (2006). This contrasts with the extremely dense forcing—dense both spatially and temporally—used in orthodox beta-turbulence studies. Such studies use a spatially dense forcing of a special kind, in order to achieve spectral narrowness [e.g., Srinivasan and Young 2014, (20) and Fig. 1f].

Sparse forcing need not, by itself, lead to sparse vortex fields in a model with numerical dissipation small enough to allow long vortex lifetimes. For isolated strong vortices having our standard size $r_0 = 4\Delta x$, injected into favorable shear, and with peak strength 16 times the shear, we find that lifetimes under numerical dissipation alone are typically on the order of years, albeit variable because they depend on the Robert filter and on bulk advection speeds across the grid (Thomson 2015, section 2.1.1).

For comparison, average injection rates are on the order of two vortex pairs per day in all the cases described above; and so the modest number of small vortices seen in snapshots like Fig. 5b can be explained only if vortex lifetimes are more like months than years. Vortex lifetimes are therefore limited not by numerical dissipation but by the chaotic vortex interactions themselves, as illustrated by the erosion and shredding events seen in the q-field movies.

The longest-lived small vortices are the anticyclones in the zone. Of these, the weakest come from local injections, corresponding to low values of the ramp function $\rho(\zeta)$, and the strongest from migration events like the two events described in section 5b. Such migration, of small but relatively strong anticyclones from belt to zone, can be attributed to a combination of chaotic, quasi-random walking away from strong-injection sites on the one hand and the so-called beta-drift or beta-gyre mechanism on the other.

b. *The beta-drift or beta-gyre mechanism*

As is well known, and as we have verified by experimentation with our model, a single vortex injected into a background PV gradient will immediately advect the background gradient to produce a pair of opposite-signed PV anomalies on either side, traditionally called beta gyres, whose induced velocity field advects the original vortex toward background values closer to its own PV values. This migration mechanism weakens as the anomalies wrap up into a spiral pattern around the original vortex. Nevertheless, the mechanism appears to have a role in helping an anticyclone to cross a jet, from belt to zone either northward or southward. Such an anticyclone typically carries with it a wrapped-up cyclonic fringe, which is subsequently eroded away.

The inward migration of injected *cyclones* within a larger cyclone plays a role in the buildup and persistence of the statistically steady large cyclones we observe. For instance, the example in the movie between $t_{\rm rel} \simeq 0.04$ and 0.10 (section 5b) does, on close inspection, show a local beta-drift mechanism in operation, the neighboring PV contours being weakly twisted in the sense required, as is especially clear around $t_{\rm rel} \simeq 0.10$. The corresponding mechanism for large anticyclones seems too weak to compete with erosion in the regimes explored so far that have realistic ζ structure.

c. *The eddy fluxes* $\overline{v'q'}$ *and* $\overline{u'v'}$

For brevity, no profiles of $\overline{v'q'}$ and $\partial(\overline{v'q'})/\partial y$ are shown here. Their qualitative characteristics are, however, simple and easy to see for realistic, statistically steady states like that of Fig. 5. For then, broadly speaking, ζ and b are maximal in midbelt and minimal in midzone, for quasi-zonal ζ fields like that in Fig. 5a. Recall that b is tied to ζ by (3.7). In a statistically steady state the right-hand side of (2.8) must vanish after sufficient time averaging. Thus averaged, $\partial(\overline{v'q'})/\partial y$ must therefore have the same y profile as $\overline{F}$. Apart from a sign reversal and an

[9] A reviewer has asked for more evidence against vortex merging and upscale energy cascading. Our best answer, beyond saying that the q-field movie described in section 5b shows typical behavior—as also seen in the output from other runs—is to call attention to the extremely long run described in section 5e. Even after 710 yr of integration, vortex merging has made no net headway against vortex erosion and shredding; and the distribution of vortex sizes remains qualitatively indistinguishable from that in Fig. 5b, including the size of the largest anticyclone. That is, all the vortices remain small in comparison with L_D apart from the single large cyclone, which persists as a coherent entity whose size is statistically steady. The other point to make is that, as will be noted in sections 6c and 6d, the upscale energy transfer responsible for strengthening the upper jets depends mainly on vortex migration, with little dependence on vortex merging, and is a direct and not a stepwise transfer from small scales to large.

additive constant, such $\overline{F}$ profiles are shaped like smoothed versions of the profiles of A in Fig. 7, in realistic cases, although $-\overline{F}$ tends to be more strongly peaked in midbelt because of the dependence (3.7) of b on ζ. The peak in $-\overline{F}$ comes from injections that are both stronger, as indicated by the midbelt peak in $A(y)$, and more strongly biased because b itself peaks in midbelt. The additive constant is required in order to make $\int_0^{2\pi L}\overline{F}\,dy = 0$ for consistency with the second equation in (2.6).

Periodicity and the Taylor identity (2.9) require, moreover, that $\int_0^{2\pi L}\overline{v'q'}\,dy = 0$. The $\overline{v'q'}$ profile therefore has to be qualitatively like an additive constant plus the periodic part of the indefinite integral of $-A(y)$. Again after sufficient time averaging this is a smooth, quasi-sinusoidal curve going positive to the south and negative to the north of midbelt, which is consistent with the migration of strong anticyclones from belt to zone already noted. Both $\overline{v'q'}$ and $\overline{u'v'}$ are upgradient at nearly all latitudes, in pure-DI cases. Explicit diagnostics of the model output confirm this qualitative picture (Thomson 2015, Figs. 4.12 and 4.13). There is no PV-mixing signature in the statistically steady state essentially because, as illustrated in Fig. 5b, the mixing has already taken place.

d. Noncascade energy transfer and quasi-frictional time scales

The upgradient migration of small anticyclones from belts to zones is crucial to the strengthening of the upper jets relative to the deep jets. It is therefore crucial to obtaining realistic belt–zone contrasts in small-scale convective activity.

The migration produces a clustering of anticyclones, on the largest possible meridional scale, into regions whose background is already anticyclonic. Energetically, this of course implies an energy transfer from vortex-injection scales directly to the largest meridional scales, as distinct from a Kolmogorovian turbulent energy cascade via intermediate scales. The direct transfer is balanced by the quasi-frictional $\overline{F}$ effect, taking the large-scale energy back out of the system.

Quasi-frictional time scales in our model are on the order of decades,[10] considerably shorter than radiative time scales near the bottom interface, which even without clouds can be estimated as more like a century [e.g., Gierasch and Goody 1969; Pierrehumbert 2010, (4.24); R. Young 2015, personal communication].

e. The large vortices in run DI-12–32–16

The run DI-12–32–16 [for details, again see Thomson (2015)] develops not only a large cyclone but also a large anticyclone, perhaps reminiscent of the real planet's Ovals, though more symmetrically located within the model zone. There are two caveats about this run. First and most important, the accompanying ζ structure is footprint dominated, and not quasi zonal as in Fig. 5a. So we count it as unrealistic. The model's large anticyclone depends less on belt-to-zone migration than on strong injections directly into the zone.

Second, the two large vortices and their periodic images form a vortex street, more precisely a doubly periodic vortex lattice, constrained by the 2:1 geometry of the model domain. Without extending our study to a much larger domain we cannot, therefore, claim to be capturing possible vortex-street properties in any natural way.

f. Runs with no deep jets

It might be asked what happens to flow regimes like that of Fig. 5, run DI-12–16–16, when the deep jets are removed while keeping everything else the same. Part of the answer is clear from inspection of the A2 stability criterion (4.1). For our standard pure-DI initial conditions, with sinusoidal $\overline{u}(y)$, removing the deep jets puts the flow well above the shear-stability threshold.

Indeed (4.1) then collapses to $k_{\min}^2 > L^{-2}$ as the condition for stability. Thus, the stability threshold becomes independent of L_D, and the initial jets are always unstable in the 2:1 domain or in any other doubly periodic domain whose zonal extent exceeds the jet spacing. The counterpropagating Rossby waves can no longer be decoupled by reducing L_D. Reducing L_D produces a precisely compensating increase in $\partial\overline{q}/\partial y$ through the term $k_D^2\overline{u}$ in (2.4). For our standard pure-DI initial conditions, therefore, the stabilization, hence straightness, of the upper jets depends on the presence of the deep jets as well as on having an L_D value that is not too large.

Runs DI-12–16–16 and DI-12–16–1 were repeated with the deep jets removed by taking $U_{\max} = 0$ in (2.3). As expected, the initial flows were then violently unstable to the longest available waves, those with wavenumber $k_{\min}$. The initial zonal jets were rapidly destroyed, leaving behind a quasi-random distribution of wandering vortices of various sizes. These included some very large vortices, one cyclone and one anticyclone per domain cell, in the

[10] For instance, run DI-12–16–16 has a quasi-frictional time scale on the order of 15 yr. It can be estimated from the steady-state quasi-frictional mean force profile for that run (minus the indefinite y integral of $\overline{F}$) in Fig. 4.12d of Thomson (2015), peaking at just over $4\times10^{-8}\,\mathrm{m\,s^{-2}}$. Noting the difference between the $b_{\max} = 1/16$ curve and the dashed curve in Fig. 3 above, peaking at just under $20\,\mathrm{m\,s^{-1}}$, we obtain a time scale around 15 yr as the ratio of the two quantities.

first of the two runs. In that run their sizes were comparable to the sizes of the large vortices in the run DI-12–32–16 described in the last subsection. However, their behavior was quite different. They wandered quasi randomly rather than being locked into a stable doubly periodic lattice. It seems that in run DI-12–32–16 the influence of the deep jets was essential to stabilizing the lattice of large vortices.

The second run, DI-12–16–1 with its deep jets removed, began similarly with a violent long-wave instability but then settled into a state whose largest vortices, all anticyclones in this case, were somewhat smaller in size and greater in number. The behavior was quite unlike that found by Li et al. (2006). We may note that Li et al. studied regimes with $b = 1$ and no deep jets but also with strong monotonic background PV gradients. Indeed their case having the most realistic jet speeds (their Fig. 9) had a β_0 value significantly enhanced by introducing a strong, $80\,\mathrm{m\,s^{-1}}$, *retrograde* deep flow $U_0 < 0$; recall (4.2).

To better understand Li et al.'s results, a set of runs was carried out with $b = 1$, monotonic background PV, no deep flow ($U_{\max} = U_0 = 0$), and other choices aimed at getting as close as possible to the conditions they studied; for more detail, see Thomson (2015, section 3.5.1 and Figs. B.1–B.9). Besides the large quasi-frictional effect for $b = 1$, two other mechanisms were found to be important: first, inhomogeneous PV mixing, converting the background PV gradient into a fairly sharp staircase giving sharp prograde jets and, second, predominantly equatorward migration of the injected anticyclones through the (still monotonic) background PV gradient. In our doubly periodic domain, this had a new effect not reported in Li et al.'s channel-domain results. The migration, predominantly equatorward out of the belts, produced a persistent phase shift in $\overline{q}(y, t)$ that gave rise to persistent poleward propagation of the jet system. That propagation is perhaps reminiscent of the downward propagation of the terrestrial quasi-biennial oscillation, though we emphasize that its mechanism is quite different. In any case, no poleward propagation of the jet system is seen on the real planet.

7. The Kelvin mechanism

The Kelvin/CE2/SSST/ZI passive-shearing mechanism has gained increased attention recently (e.g., Srinivasan and Young 2014 and references therein). It is one of three very different mechanisms for creating and sharpening jets, the other two being the Rhines and PV-mixing mechanisms already mentioned. The Kelvin mechanism is simple to understand, especially when the weak forcing is anisotropic in the same sense as that of our injected vortex pairs, with their east-to-west orientation. Such pairs are immediately sheared into phase-tilted structures producing upgradient Reynolds stresses $\overline{u'v'}$. The Taylor identity (2.9) determines the accompanying $\overline{v'q'}$ field. That field describes an eddy PV flux that is upgradient at some latitudes y and downgradient at others and, as indicated by the y derivative in (2.9), involves subtle phase relations sensitive to the y gradients of disturbance amplitude and shearing rates.

To suppress small-scale vortex activity and to allow the Kelvin mechanism to dominate, we must take $q^*_{\max}$ small enough to ensure that injections are almost always weak. Figures 10–12 show statistically steady $\overline{u}$, $\overline{\zeta}$, and $\overline{q}$ profiles from a pair of pure-DI runs with $q^*_{\max} = 0.5$ and 1 (dark and light curves, respectively), the runs labeled DI-12–0.5–64 and DI-12–1–64. As before, we take $L_D = 1200\,\mathrm{km}$. The Kelvin mechanism is so weak that, in order to see it working and to reach statistical steadiness, we had to reduce $b_{\max}$ to 1/64 and increase the average injection rate by two orders of magnitude (i.e., we had to reduce $t_{\max}$ by a factor 100), as specified in the caption to Table 1.

The jets are indeed sharpened and the jet-core $\overline{q}$ profiles steepened in both cases, creating in turn a $\overline{\zeta}$ structure that is interesting but unrealistic. As Fig. 11 shows, the central part of the belt is relatively warm, $\overline{\zeta}$ negative, with only the edges cold, $\overline{\zeta}$ positive. The corresponding A profiles from (5.1) are given in Fig. 13, showing an inhibition of convective activity in midbelt. No such inhibition is seen on the real planet.

The unrealistic $\overline{\zeta}$ structure arises from the way the Kelvin mechanism works in a model with no artificial Rayleigh friction, corresponding to the low-friction limit found by Srinivasan and Young (2014), their $\mu \to 0$. Each sheared vortex-pair structure survives as long as it can, through nearly the whole range of phase-tilt angles. It is only when the orientation has become nearly zonal that the structure is destroyed by the model's high-wavenumber filter. Thus, its lifetime is inversely proportional to the local background shear $\partial\overline{u}/\partial y$. The Reynolds stress $\overline{u'v'}$, time averaged over many injections, is also, therefore, inversely proportional to $\partial\overline{u}/\partial y$, as in (44) of Srinivasan and Young (2014). So as long as the $\overline{u}$ profile remains close to its initially sinusoidal shape while the ζ field remains flat, keeping injection strengths uniform everywhere, the profile of $-\overline{u'v'}$ has a smooth, positive-valued U shape within the belt, with a broad minimum in midbelt and a steep increase toward each jet extremum. In the zone, with the sign of $\partial\overline{u}/\partial y$ reversed, it is $+\overline{u'v'}$ rather than $-\overline{u'v'}$ that is positive and U shaped. Therefore, there is a very steep transition at each jet extremum producing a sharp, narrow peak in the zonal force $-\partial(\overline{u'v'})/\partial y$, positive at the prograde jet and negative at the retrograde jet.

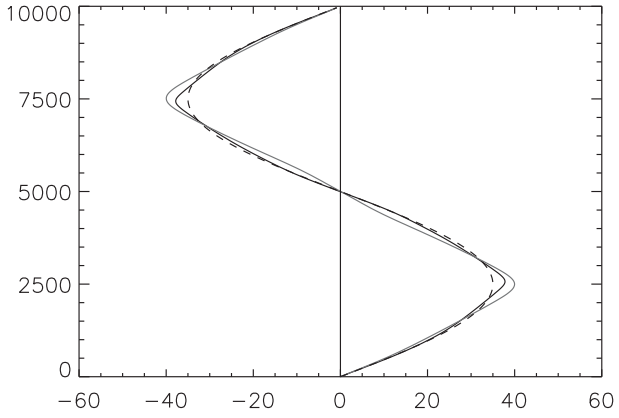

FIG. 10. Zonal-mean zonal velocity profiles $\overline{u}(y)$ (m s^{-1}; y axis in kilometers) for a pair of Kelvin-dominated, pure-DI runs DI-12–0.5–64 and DI-12–1–64 with $L_D = 1200$ km and $q^*_{\max} = 0.5$ (dark solid curve) and $q^*_{\max} = 1.0$ (light solid curve), with $b_{\max} = 1/64$ and with injection rates $t^{-1}_{\max}$ increased by a factor 100, as specified in the caption to Table 1. Although it makes little difference to these profiles, they have been time averaged from $t = 108$ to 202 Earth years for consistency with the profiles of $\overline{\zeta}$, $\overline{q}$, and A shown below, some of which are more subject to fluctuations within a statistically steady state. The dashed curve is the deep-jet velocity profile $\overline{u}_{\text{deep}}(y) - U_0$ as before.

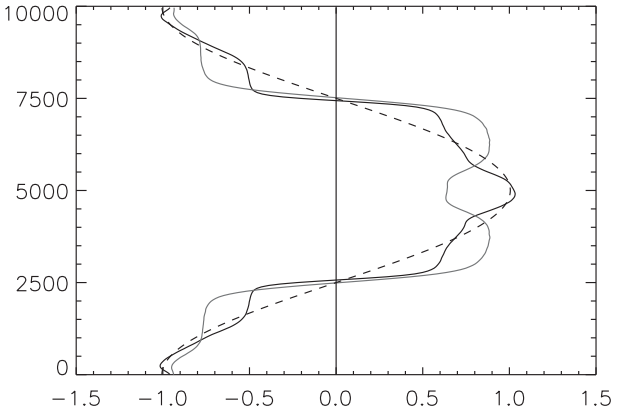

FIG. 12. Zonal-mean PV profiles $\overline{q}(y)$ (y axis in kilometers) for the same pair of Kelvin-dominated runs, with $q^*_{\max} = 0.5$ (dark solid curve) and $q^*_{\max} = 1.0$ (light solid curve), both time averaged from $t = 108$ to 202 Earth years as in Fig. 10; see text. The dashed, sinusoidal curve is the initial PV profile. The PV is in units of $U_{\max}/L = 2.199 \times 10^{-5}$ s^{-1} as before.

The jet sharpening is therefore strongly localized. It begins with narrow peaks growing at the extrema of the otherwise-sinusoidal $\overline{u}$ profile, with $|\partial\overline{u}/\partial y|$ reduced everywhere else. The PV profile develops correspondingly sharp steps, cut into the sides of its initially sinusoidal shape. That is, there is localized jet sharpening but—in striking contrast with Fig. 3—weakening rather than strengthening of $\overline{u}$ at most other latitudes y. The thermal wind tilt of the interface is therefore, at most other latitudes, opposite to what it was in the cases discussed in section 5, except within narrow regions near the jet peaks. That is the essential reason why the belt develops a warm, negative-$\overline{\zeta}$ central region with cold, positive-$\overline{\zeta}$ regions only in the outer parts of the belt.

The change in the y profile of $\overline{\zeta}$ and hence of injection strengths then reacts back on the $\overline{u'v'}$ profiles, but in a rather smooth way that leaves the qualitative pattern unchanged. Indeed, the back reaction acts as a positive feedback that *reinforces* the pattern, because the warm belt center weakens the injections there and thus deepens the central minimum in the U-shaped profile of

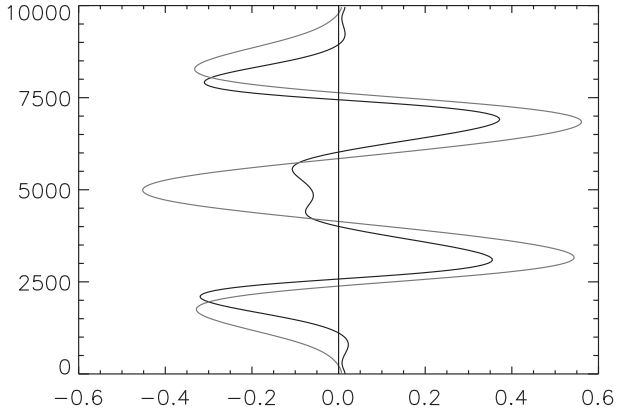

FIG. 11. Zonal-mean interface-elevation profiles $\overline{\zeta}(y)$ (y axis in kilometers) for the same pair of Kelvin-dominated runs, with $q^*_{\max} = 0.5$ (dark curve) and $q^*_{\max} = 1.0$ (light curve), both time averaged from $t = 108$ to 202 Earth years as in Fig. 10. Without the time averaging, the $q^*_{\max} = 1.0$ curve would be less symmetric and would fluctuate noticeably because of vacillations mentioned in the text.

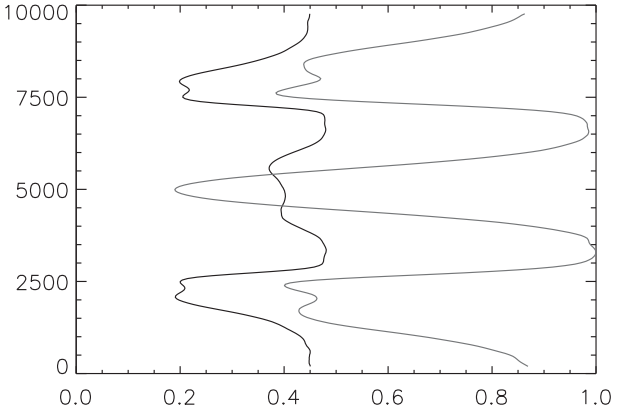

FIG. 13. Relative moist-convective activity profiles $A(y)/A_{\max}$ (y axis in kilometers) from (5.1) for the same pair of Kelvin-dominated runs, with $q^*_{\max} = 0.5$ (dark curve) and $q^*_{\max} = 1.0$ (light curve), both time averaged from $t = 108$ to 202 Earth years as in Fig. 10. In the central part of the belt, convective activity is inhibited for the reasons explained in the text.

$-\overline{u'v'}$. That is why the light curve in Fig. 10, corresponding to the less weakly forced run, $q^*_{\max} = 1$, shows a $\overline{u}$ profile more conspicuously weakened across most of the belt. The resulting thermal wind tilt further reinforces the central warmth of the belt.

The stronger feedback for $q^*_{\max} = 1$ appears to be responsible for the central dip in the $\overline{q}$ profile seen in the light curve in Fig. 12. The central dip gives rise to a weak long-wave shear instability (though stronger when $L_D = 1500$ km), because we then have nonmonotonic $\partial\overline{q}/\partial y$ on a smaller y scale, putting pairs of counterpropagating Rossby waves within reach of each other. This long-wave instability produces vacillations in the form of weak traveling undulations with zonal wavenumber 1. The vacillations hardly affect the $\overline{u}$ and $\overline{q}$ profiles but show up more clearly in a time sequence of $\overline{\zeta}$ profiles. The corresponding $\overline{\zeta}$ profile in Fig. 11 (light curve) has been time averaged to reduce the effects of these vacillations.

For $q^*_{\max} = 0.5$, we see a weak and entirely different, zonally symmetric, mode of instability that causes spontaneous y-symmetry breaking in the central region of the belt, $4000 \lesssim y \lesssim 6000$ km. For instance, the $\overline{u}$ profile given by the dark solid curve in Fig. 10 shows a tiny departure from antisymmetry about midbelt. The dark curves in Figs. 11 and 13 are more conspicuously asymmetric in the central region. Considering a $\overline{u}$ profile consisting of a constant cyclonic shear plus a small wavy perturbation, we see that such a perturbation is zonostrophically stable—because the abovementioned inverse proportionality reduces $|\overline{u'v'}|$ wherever $|\partial\overline{u}/\partial y|$ increases—but "thermostrophically unstable" via the feedback from $\overline{\zeta}$, which evidently has the opposite effect on $|\overline{u'v'}|$ and predominates in this case.

8. Concluding remarks

In view of the Kelvin regime's lack of realism we return to the model's realistic, statistically steady, pure-DI regimes that have been our main focus (sections 5 and 6). In those regimes, not only is $\overline{u'v'}$ persistently upgradient, but also $\overline{v'q'}$, at nearly all latitudes y, after sufficient time averaging. The small-scale vortex activity produces a persistent migration of small anticyclones from belts to zones. It is this upgradient migration that *strengthens* the upper jets, as distinct from the inhomogeneous PV mixing that *sharpens* them. The importance of migration on the real planet was suggested by Ingersoll et al. (2000). In the model it is mediated by quasi-random walking away from strong-injection sites, via chaotic vortex interactions, in combination with the beta-drift mechanism (section 6b above).

Both mechanisms are entirely different from the Kelvin jet-sharpening mechanism because the latter involves no vortex activity, as already emphasized, but only passive shearing of injected vortex pairs by the background zonal flow $\overline{u}(y)$. Passive shearing of small-scale anomalies is also what seems to produce the upgradient $\overline{u'v'}$ in the real planet's cloud-top winds (e.g., Salyk et al. 2006). Yet, in our model at least, as shown in section 7, the Kelvin mechanism cannot produce a realistic ζ structure. It therefore cannot, in this model, produce a realistic belt–zone contrast in moist-convective activity.

We suggest therefore that the cloud-top $\overline{u'v'}$ on the real planet must be a relatively shallow phenomenon, whose vertical scale is much smaller than the depth of the weather layer. It is most likely, we suggest, to result not from the shearing of tall, columnar vortices resembling the injected vortices in our model but, rather, from the shearing of the real weather layer's small-scale, baroclinic, fully three-dimensional fluid motions. Such motions, including shallow vortices and the real filamentary moist convection are, of course, outside the scope of any 1½-layer model and not simply related to PV fields like that of Fig. 5b above.

As is well known, the same conclusions are suggested by the implausibly large kinetic energy conversion rates obtained when the cloud-top $\overline{u'v'}$ field is assumed to extend downward, along with $\partial\overline{u}/\partial y$, throughout the entire weather layer. When one vertically integrates cloud-top conversion rates $\overline{u'v'}\partial\overline{u}/\partial y$, whose global average is on the order of $10^{-4}\,\mathrm{W\,kg^{-1}}$, then global integration gives numbers "in the range 4%–8% of the total thermal energy emitted by Jupiter" (Salyk et al. 2006, and references therein). Such large conversion rates are overwhelmingly improbable in a low-Mach-number fluid system such as Jupiter's weather layer.

Consistent with these considerations, the model's flow regimes with realistic ζ structures have conversion rates $\overline{u'v'}\partial\overline{u}/\partial y$ that are still positive but are about two orders of magnitude smaller. For instance, in the case examined in section 5b we find $\overline{u'v'}\partial\overline{u}/\partial y$ values that fluctuate around a time mean close to $1 \times 10^{-6}\,\mathrm{W\,kg^{-1}}$ (Thomson 2015, Fig. 4.13). Such values are much more plausible, for the whole weather layer, than the observed cloud-top values around $10^{-4}\,\mathrm{W\,kg^{-1}}$.

As well as the model's success in producing flow regimes with realistically straight weather-layer jets and realistic, internally generated belt–zone contrasts in moist-convective activity, we note again the implied restriction on L_D values. Such a restriction holds in the model and also, very probably, on the real planet. In the model, we found that realistic behavior requires

$L_D \lesssim 1500$ km at 35° latitude. It therefore seems probable that values such as the 5000 km used for all the midlatitude flow fields presented in Li et al. (2006), for instance, are unrealistically large.

Perhaps the weakest aspect of the current model is the artificial condition (3.10) that we adopted in order to avoid strong-cyclone runaway. As is well known, the real planet's large cyclones can be intensely convective, presumably because they have cold, high-ζ footprints. No 1½-layer vortex-injection scheme can come close to representing the three-dimensional reality. An attractive compromise, and a possible way of dispensing with (3.10), might be to introduce an eddy viscosity whose value intensifies whenever and wherever the model's convective activity intensifies. This might capture some of the dissipative effects of the real, three-dimensionally turbulent moist convection while still avoiding the use of Rayleigh friction or other such artifice.

A localized, convection-dependent eddy viscosity would have the advantage of, probably, allowing realistic statistically steady states with a simpler vortex-injection scheme, such as that described by (3.2)–(3.9) alone. It could automatically expand the core sizes, and dilute the peak strengths, of the strongest injected vortices and thus prevent strong-cyclone runaway. As an added bonus, it might even produce realistic cases in which large anticyclones form (cf. section 6e). Because the real planet's large anticyclones are not ubiquitous, there may be a certain delicacy about the conditions that allow them to form.

Such questions must await future studies. These could include studies using general circulation models in which the lower boundary conditions, about which there is so much uncertainty, are replaced by conditions corresponding to a flexible interface above prescribed deep jets.

Acknowledgments. Emma Boland and Andy Thompson kindly helped us with the model code. We also thank them for useful comments and and/or encouragement along with James Cho, Tim Dowling, David Dritschel, Leigh Fletcher, Boris Galperin, Thomas Gastine, Gary Glatzmaier, Peter Haynes, Xianglei Huang, Andy Ingersoll, Chris Jones, Kirill Kuzanyan, Junjun Liu, Inna Polichtchouk, Peter Read, Tapio Schneider, Richard Scott, Sushil Shetty, Adam Showman, Steve Tobias, Richard Wood, Bill Young, and Roland Young. The paper's reviewers suggested many useful clarifications, for which we are grateful. We also thank the U.K. Science and Technology Facilities Council for financial support in the form of a research studentship.

REFERENCES

Asay-Davis, X. S., P. S. Marcus, M. H. Wong, and I. de Pater, 2009: Jupiter's shrinking Great Red Spot and steady Oval BA: Velocity measurements with the 'Advection Corrected Correlation Image Velocimetry' automated cloud-tracking method. *Icarus*, **203**, 164–188, doi:10.1016/j.icarus.2009.05.001.

Bühler, O., 2014: *Waves and Mean Flows*. 2nd ed. Cambridge University Press, 360 pp., doi:10.1017/CBO9781107478701.

Dowling, T. E., 1993: A relationship between potential vorticity and zonal wind on Jupiter. *J. Atmos. Sci.*, **50**, 14–22, doi:10.1175/1520-0469(1993)050<0014:ARBPVA>2.0.CO;2.

——, and A. P. Ingersoll, 1989: Jupiter's Great Red Spot as a shallow water system. *J. Atmos. Sci.*, **46**, 3256–3278, doi:10.1175/1520-0469(1989)046<3256:JGRSAA>2.0.CO;2.

Gastine, T., M. Heimpel, and J. Wicht, 2014: Zonal flow scaling in rapidly-rotating compressible convection. *Phys. Earth Planet. Inter.*, **232**, 36–50, doi:10.1016/j.pepi.2014.03.011.

Gierasch, P. J., and R. M. Goody, 1969: Radiative time constants in the atmosphere of Jupiter. *J. Atmos. Sci.*, **26**, 979–980, doi:10.1175/1520-0469(1969)026<0979:RTCITA>2.0.CO;2.

Guillot, T., 2005: The interiors of giant planets: Models and outstanding questions. *Annu. Rev. Earth Planet. Sci.*, **33**, 493–530, doi:10.1146/annurev.earth.32.101802.120325.

Haynes, P. H., and M. E. McIntyre, 1990: On the conservation and impermeability theorems for potential vorticity. *J. Atmos. Sci.*, **47**, 2021–2031, doi:10.1175/1520-0469(1990)047<2021:OTCAIT>2.0.CO;2.

Hoskins, B., M. McIntyre, and A. Robertson, 1985: On the use and significance of isentropic potential-vorticity maps. *Quart. J. Roy. Meteor. Soc.*, **111**, 877–946, doi:10.1002/qj.49711147002; Corrigendum, **113**, 402–404, doi:10.1002/qj.49711347522.

Humphreys, T., and P. S. Marcus, 2007: Vortex street dynamics: The selection mechanism for the areas and locations of Jupiter's vortices. *J. Atmos. Sci.*, **64**, 1318–1333, doi:10.1175/JAS3882.1.

Ingersoll, A. P., and C. C. Porco, 1978: Solar heating and internal heat flow on Jupiter. *Icarus*, **35**, 27–43, doi:10.1016/0019-1035(78)90058-1.

——, and P. Cuong, 1981: Numerical model of long-lived Jovian vortices. *J. Atmos. Sci.*, **38**, 2067–2076, doi:10.1175/1520-0469(1981)038<2067:NMOLLJ>2.0.CO;2.

——, and Coauthors, 2000: Moist convection as an energy source for the large-scale motions in Jupiter's atmosphere. *Nature*, **403**, 630–632, doi:10.1038/35001021.

Jones, C. A., and K. M. Kuzanyan, 2009: Compressible convection in the deep atmospheres of giant planets. *Icarus*, **204**, 227–238, doi:10.1016/j.icarus.2009.05.022.

Kida, S., 1981: Motion of an elliptic vortex in a uniform shear flow. *J. Phys. Soc. Japan*, **50**, 3517–3520, doi:10.1143/JPSJ.50.3517.

Li, L., A. P. Ingersoll, and X. Huang, 2006: Interaction of moist convection with zonal jets on Jupiter and Saturn. *Icarus*, **180**, 113–123, doi:10.1016/j.icarus.2005.08.016.

Limaye, S. S., 1986: Jupiter: New estimates of the mean zonal flow at the cloud level. *Icarus*, **65**, 335–352, doi:10.1016/0019-1035(86)90142-9.

Liu, J., T. Schneider, and Y. Kaspi, 2013: Predictions of thermal and gravitational signals of Jupiter's deep zonal winds. *Icarus*, **224**, 114–125, doi:10.1016/j.icarus.2013.01.025.

Marcus, P. S., and S. Shetty, 2011: Jupiter's zonal winds: Are they bands of homogenized potential vorticity organized as a monotonic staircase? *Philos. Trans. Roy. Soc. London*, **A369**, 771–795, doi:10.1098/rsta.2010.0299.

Maximenko, N. A., B. Bang, and H. Sasaki, 2005: Observational evidence of alternating zonal jets in the world ocean. *Geophys. Res. Lett.*, **32**, L12607, doi:10.1029/2005GL022728.

McIntyre, M. E., and T. G. Shepherd, 1987: An exact local conservation theorem for finite-amplitude disturbances to non-parallel shear flows, with remarks on Hamiltonian structure and on Arnol'd's stability theorems. *J. Fluid Mech.*, **181**, 527–565, doi:10.1017/S0022112087002209.

Pierrehumbert, R. T., 2010: *Principles of Planetary Climate.* Cambridge University Press, 652 pp.

Porco, C. C., and Coauthors, 2003: Cassini imaging of Jupiter's atmosphere, satellites, and rings. *Science*, **299**, 1541–1547, doi:10.1126/science.1079462.

Read, P. L., P. J. Gierasch, B. J. Conrath, A. Simon-Miller, T. Fouchet, and Y. H. Yamazaki, 2006: Mapping potential-vorticity dynamics on Jupiter. I: Zonal-mean circulation from Cassini and Voyager 1 data. *Quart. J. Roy. Meteor. Soc.*, **132**, 1577–1603, doi:10.1256/qj.05.34.

Salyk, C., A. P. Ingersoll, J. Lorre, A. Vasavada, and A. D. Del Genio, 2006: Interaction between eddies and mean flow in Jupiter's atmosphere: Analysis of Cassini imaging data. *Icarus*, **185**, 430–442, doi:10.1016/j.icarus.2006.08.007.

Scott, R. K., and L. M. Polvani, 2007: Forced-dissipative shallow-water turbulence on the sphere and the atmospheric circulation of the giant planets. *J. Atmos. Sci.*, **64**, 3158–3176, doi:10.1175/JAS4003.1.

Shepherd, T. G., 1985: Time development of small disturbances to plane Couette flow. *J. Atmos. Sci.*, **42**, 1868–1871, doi:10.1175/1520-0469(1985)042<1868:TDOSDT>2.0.CO;2.

Shetty, S., and P. S. Marcus, 2010: Changes in Jupiter's Great Red Spot (1979–2006) and Oval BA (2000–2006). *Icarus*, **210**, 182–201, doi:10.1016/j.icarus.2010.06.026.

Showman, A. P., 2007: Numerical simulations of forced shallow-water turbulence: Effects of moist convection on the large-scale circulation of Jupiter and Saturn. *J. Atmos. Sci.*, **64**, 3132–3157, doi:10.1175/JAS4007.1.

——, and I. de Pater, 2005: Dynamical implications of Jupiter's tropospheric ammonia abundance. *Icarus*, **174**, 192–204, doi:10.1016/j.icarus.2004.10.004.

Smith, K. S., G. Boccaletti, C. C. Henning, I. Marinov, C. Y. Tam, I. M. Held, and G. K. Vallis, 2002: Turbulent diffusion in the geostrophic inverse cascade. *J. Fluid Mech.*, **469**, 13–48, doi:10.1017/S0022112002001763.

Srinivasan, K., and W. R. Young, 2012: Zonostrophic instability. *J. Atmos. Sci.*, **69**, 1633–1656, doi:10.1175/JAS-D-11-0200.1.

——, and ——, 2014: Reynolds stress and eddy diffusivity of β-plane shear flows. *J. Atmos. Sci.*, **71**, 2169–2185, doi:10.1175/JAS-D-13-0246.1.

Stamp, A., and T. E. Dowling, 1993: Jupiter's winds and Arnol'd's second stability theorem: Slowly moving waves and neutral stability. *J. Geophys. Res.*, **98**, 18 847–18 855, doi:10.1029/93JE01520.

Sugiyama, K., M. Odaka, K. Kuramoto, and Y.-Y. Hayashi, 2006: Static stability of the Jovian atmospheres estimated from moist adiabatic profiles. *Geophys. Res. Lett.*, **33**, L03201, doi:10.1029/2005GL024554.

——, K. Nakajima, M. Odaka, K. Kuramoto, and Y.-Y. Hayashi, 2014: Numerical simulations of Jupiter's moist convection layer: Structure and dynamics in statistically steady states. *Icarus*, **229**, 71–91, doi:10.1016/j.icarus.2013.10.016.

Thomson, S. I., 2015: A new model of Jupiter's jet streams and the effects of moist convection. Ph.D. thesis, University of Cambridge, 227 pp.

Thomson, W., 1887: Stability of fluid motion—Rectilineal motion of viscous fluid between two parallel planes. *Philos. Mag.*, **24**, 188–196, doi:10.1080/14786448708628078.

Vallis, G. K., G. J. Shutts, and M. E. B. Gray, 1997: Balanced mesoscale motion and stratified turbulence forced by convection. *Quart. J. Roy. Meteor. Soc.*, **123**, 1621–1652, doi:10.1002/qj.49712354209.

Walterscheid, R., 2000: Wave disturbances from the Comet SL-9 impacts into Jupiter's atmosphere. *Icarus*, **145**, 140–146, doi:10.1006/icar.1999.6334.